

ABSTRACT

Title of Thesis:

**RB-SR RADIOMETRIC DATING OF
ROCKY PLANETARY BODIES VIA LA-
ICPMS**

Kiran Shahood Almas, Master of Science, 2021

Thesis Directed By:

Dr. Ricardo Arevalo, Jr. (Associate Professor)
Department of Geology

Constraining ages of surface features on rocky objects in the Solar System provides fundamental insights about the flux of impactors through time (including the putative Late Heavy Bombardment), rates of tectonic and volcanic processes, and temporal context for detected organic compounds. Spaceflight instrumentation is being developed to characterize these ages *in situ*. An LA-ICPMS is suggested as a candidate for a planetary chronology mission, with Mars as a case study; the capability of the technique to measure Rb and Sr isotopic signatures in geological samples with adequate accuracy within the 200 Myr (2σ) precision benchmark presented in NASA's Technology Roadmap is tested. Data are presented that reports on these metrics for $^{87}\text{Sr}/^{86}\text{Sr}$ ratios, and a Monte Carlo simulation models synthetic isochrons to evaluate the accuracy and precision limitations of this method. A minimum of 10 data points per sample is suggested to meet the NASA benchmark.

RB-SR RADIOMETRIC DATING OF ROCKY PLANETARY BODIES VIA
LA-ICPMS

by

Kiran Shahood Almas

Thesis submitted to the Faculty of the Graduate School of the
University of Maryland, College Park, in partial fulfillment
of the requirements for the degree of
Master of Science
2021

Advisory Committee:

Associate Professor Ricardo Arevalo, Jr., Chair
Assistant Professor Megan Newcombe, Member
Research Scientist Philip Piccoli, Member

© Copyright by
Kiran Shahood Almas
2021

Acknowledgements

This document would not have been completed if it weren't for the constant support from my family, friends, and colleagues.

I have to begin by thanking my family. Like all mothers, my mom has sacrificed a lot for me. The life I have now isn't the one she envisioned for me, but she is still supportive to a fault, and for that I can never appreciate her enough. To all the mother figures in my life, thank you for finding space for me and loving me like one of your own. To my grandfather, who has always reminded me of the importance of a good education and of knowing your tenses, thank you for teaching me at a(n arguably too) young age all the math I'd need to learn for the first ten years of my life. Although he doesn't understand why I'd choose to associate with rocks or how my life led me here, he trusts me to know what I'm doing (perhaps that trust is misplaced, who knows; only time will tell). To my grandmother, who has given me my last name and has passed down some of her ancestral knowledge to me, thank you for reminding me of the strong generations of women I come from and for being a living example of a gentle but tough matriarch.

To my sister, who is my biggest critic but loves me the most. I've had to spend most of her life away from her, but she is still understanding and encourages me to never settle. Thank you for being my light and for always reminding me that there is a path home. I love you to Scooby Doo and Pluto.

Next I would like to thank my friends. Rachel Slank, thanks for being the best roommate and cave buddy; your support and guidance helped me get to graduate

school. My friends from home (Brittany Tompkins, Jay Chittidi, George Georgiou, and Rachel Ludwig) deserve all the appreciation for maintaining our friendship despite the infrequency of our conversations.

My plants (especially my Hoya Bilobata) have reminded me of the importance of staying hydrated and getting some sunlight. Watching them grow has been such an encouragement. My cat, Raat ki Rani Maryam Almas, affectionately called Rani Pani at times, has been the reason this document was compiled. Her ambition as a young kitten inspired me to make changes in my life to prioritize my happiness. She probably deserves to be a co-author on this thesis (if not the primary author)

My cohort has supported me through this ordeal, and many have become very close friends. My very first grad school friend, Heidi Myers, has changed my life in more ways than I can express. Thank you for always being a text away. Christiana Hoff, first as my TA and then as a friend, has supported me and talked me through every single moment of self-doubt I experienced in my first year in the program. Lori Willhite has been a constant friend and someone I look up to for advice and for laughter. Karla Nunez has been a great roommate and plant whisperer, and I am very grateful for all the times she asked me about my sister or pushed me out of the house for a walk when I had been working for too long. Aisha Khatib has been a kind presence in my life and has made this department feel more comfortable.

My lab group has been there for me from the very beginning. Grace Ni, Ben Farcy, and Laura Sammon have held my hand throughout this process and were instrumental in my geology education. Madeline Raith has been instrumental in

walking me through the ins and outs of linear regression models and shared her Matlab script for a York regression with me, which was used in this project.

My professors have been very kind and patient with me as I caught up on everything geology. The care with which they taught me, gently expecting a lot from me while making sure I have the resources I need, was invaluable. Thank you to Richard Walker, Michael Evans, Ricardo Arevalo, Jr., Laurent Montesi, Sarah Penniston-Dorland, Vedran Lekic, and Megan Newcombe. To Philip Piccoli, thank you for always asking me questions that I don't know the answers to; I have learned a lot through our conversations. You have taught me that saying that I don't know something is not something to be ashamed of. To Ricardo Arevalo, thank you for supporting me when I came in knowing nothing about rocks and teaching me about the amazing world of geochemistry.

To Jaime Del Razo, Colette Salyk, Colette Cann, Kimberly Williams-Brown, and Debra Elmegreen, thank you for supporting me through my undergraduate years and encouraging me to follow my dreams.

To my committee, Ricardo Arevalo, Jr., Megan Newcombe, and Philip Piccoli, thank you for supporting me through this process and guiding me through this project. Each one of you has taught me so much, and I hope this document reflects that.

To the KArLE team, thank you for teaching me about spaceflight instrumentation and allowing me to join you. Thank you to my funding sources. Most of this thesis was made possible by NASA DALI Grant #80NSSC19K1398 and by the University of Maryland.

Last, but never least, I need to thank the undo button. It came in handy every time my cat decided to waltz across my keyboard and add strange words to this thesis.

Table of Contents

Acknowledgements.....	ii
Table of Contents.....	vi
List of Tables.....	vii
List of Figures.....	viii
Chapter 1: Introduction.....	1
Motivation.....	1
Crater Counting.....	1
Dating Meteorites.....	2
Proposal.....	3
Radiometric Systems.....	3
K-Ar.....	4
Rb-Sr.....	5
Mars as a Case Study.....	7
Chapter 2: Methodology.....	11
Hardware.....	11
Analytical Techniques.....	15
Chapter 3: Results.....	17
Optimizing Analytical Parameters.....	17
Data Preprocessing.....	23
Data Processing.....	25
Accuracy and Precision.....	27
Chapter 4: Discussion and Conclusions.....	32
Extrapolating to Higher $^{87}\text{Rb}/^{86}\text{Sr}$ Ratios.....	32
Synthetic Isochron.....	34
Conclusions.....	38
Future Work.....	39
Appendix A.....	41
Appendix B.....	44
Bibliography.....	45

List of Tables

Table 1: Isobaric interferences in the mass range of interest. 13

Table 2: Operating conditions for the mass spectrometer..... 16

Table A1: Table with analysis numbers, sample name, and information on spot size to accompany the information shared in this thesis..... 43

List of Figures

Figure 1	Timeline of major events in Martian history.	8
Figure 2	Schematic of a Nu AttoM setup. From Olesik, 2014.	12
Figure 3	Range of configurations tested in the preliminary aspects of the study.	17
Figure 4	Sample chromatograms for NIST 610 and BHVO-2G.	19
Figure 5	Precision vs fluence for configurations.	20
Figure 6	$2\sigma_m$ of raw $^{87}\text{Sr}/^{86}\text{Sr}$ ratios vs combinations of repetition rate and fluence.	22
Figure 7	Effect of smoothing on accuracy and precision.	24
Figure 8	Flowchart showing the steps taken to calculate $^{87}\text{Sr}/^{86}\text{Sr}$ ratios.	25
Figure 9	Normalized $^{87}\text{Sr}/^{86}\text{Sr}$	30
Figure 10	Normalized $^{85}\text{Rb}/^{88}\text{Sr}$	31
Figure 11	$2\sigma_m$ of $^{87}\text{Sr}/^{86}\text{Sr}$ ratios regressed against the accepted $^{87}\text{Rb}/^{86}\text{Sr}$ ratios.	33
Figure 12	Sample isochrons.	35
Figure 13	Precision and accuracy of inferred age.	37

Chapter 1: Introduction

Motivation

Crater Counting

Through an extensive study of crater densities on the Moon, chronologists developed a system to determine relative ages of lunar morphological features and crustal materials. In general, the more craters a surface feature has, the older the terrain is relative to those with fewer craters (given exposure to the same impactor flux). Crater superposition is well recorded and preserved on planetary bodies that experience little to no resurfacing events, such as the Moon and Mercury. In contrast, the chronological records of geologically active bodies, such as Mars, are more difficult to interpret because of crater erasure via erosion, aqueous alteration, and aeolian-based weathering over time (Hartmann and Neukum, 2001; Greeley et al., 2001, and references therein).

Although crater counting is useful for determining the order in which formative events proceeded on a single body, the technique is not a viable method of deriving the exact age of a specific surface feature (Hartmann and Neukum, 2001; Neukum et al., 2001, and references therein). The return of lunar samples from the Apollo and Luna missions enabled quantitative constraints to be applied to the chronology of the Moon based on laboratory analyses of radioactive and radiogenic isotopes present in these rocks. Correlating absolute ages with observations of the

distribution of craters with similar diameters enabled calibration of the lunar crater record (Neukum and Horn, 1976). However, the crater records of other bodies are not as simple, as samples have not been returned yet from any other rocky objects in the Solar System with few exceptions (*e.g.*, select Martian meteorites and samples recently returned from Hayabusa2), limiting ground-truth analyses. Attempts have been made to use the lunar crater calibration to interpret the ages of Martian craters, but such models depend on a variety of uncertain parameters, such as the impactor flux at farther heliocentric distances, rates of crater erasure, *etc.*, resulting in estimated ages with large uncertainties (see Werner and Tanaka, 2011; Platz et al., 2013; and Benedix et al., 2020 for some recent examples).

Dating Meteorites

An alternative method of establishing the ages of extraterrestrial materials is through the dating of meteorites via radiometric isotope systems (described further below), but challenges remain. While dating meteorite samples may provide quantitative constraints on the age of the parent body, the geological context of these materials is often difficult to discern. An individual meteorite may have been heated and/or altered after its expulsion from its parent body, possibly resetting the isotopic systems targeted in the laboratory. There is also a limited supply of meteorites accessible to the scientific community, particularly materials derived from the Moon or Mars, thereby minimizing the number of studies that can be completed on these valuable samples.

Proposal

Thus, there is a clear and present need for *in situ* planetary chronology missions to help characterize the ages of materials and morphological features on other rocky bodies. Such missions have the capacity to provide temporal constraints on important events in the timeline of the inner Solar System. The 2015 NASA Technology Roadmap stresses the importance of *in situ* dating on rocky objects such as Mars, Vesta, and the Moon. This community document also specifies the need for measurements with a precision better than ± 200 Ma (2σ) in order to add confidence to the Solar System timeline and critically evaluate the putative late heavy bombardment. Here, a method for dating Martian samples (and other planetary materials) *in situ* is proposed: accessing the Rb-Sr radiometric system via Laser Ablation-Inductively Coupled Plasma Mass Spectrometry (LA-ICPMS). The analytical technique described here leverages technologies available for future landed missions, as described below.

Radiometric Dating

There are a multitude of radiometric systems commonly used for geochronology purposes. While some of these may yield precise ages that meet or exceed the requirements of the NASA Technology Roadmap, not all chronometers have a clear pathway to spaceflight applications. For example, the U-Pb system is routinely used to date chondritic meteorites and terrestrial zircons with the highest precision (due to multiple independent decay schemes), but the low abundances of U and Pb in most silicate minerals limit the accessibility of this system, as spaceflight instruments often do not have the same detection limits as their commercial analogs

(Arevalo et al., 2020 and references therein). Similarly, the ^{147}Sm - ^{143}Nd system can be used to date crustal samples as well as establish provenance of mantle-derived materials, but this system is also not well suited for a spaceflight mission. While both Sm and Nd are fluid-immobile, providing robustness against alteration and some degree of metamorphism, both elements exhibit similar geochemical behaviors, limiting fractionation during silicate differentiation. Limited spread in Sm/Nd, along with ^{147}Sm having a long half-life ($t_{1/2} = 106$ Gyr), lead to this system producing only small variations in $^{143}\text{Nd}/^{144}\text{Nd}$ ratios as a function of time, challenging detection capabilities.

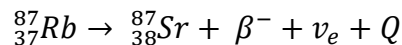
K-Ar

The K-Ar decay scheme, a particularly useful chronometer for feldspar and mica-rich lithologies, is one of the few systems that can be measured with modern day spaceflight technologies; a coordinated *in situ* analysis by the instruments on the MSL Curiosity Rover successfully enabled a model age of a 4.21 ± 0.35 (1σ) Ga for a mudstone sample *in situ* (Farley et al., 2014). However, the K-Ar system is not commonly targeted in commercial laboratories due to the need for multiple analytical techniques, namely: gas source mass spectrometry (GSMS) to measure Ar; and, isotope dilution thermal ionization mass spectrometry (TIMS) or multicollector ICPMS to measure K (Kelley, 2002). This limitation is also true for spaceflight applications. For example, the MSL experiment required the participation of three independent instruments, the Alpha Particle X-ray Spectrometer (APXS), x-ray diffraction and fluorescence instrument (CheMin), and quadrupole mass analyzer (SAM; Martin et al., 2017). Because these instruments were not specifically designed

to work together, the propagated uncertainty of the *in situ* measurement fell outside the objectives of the NASA Technology Roadmap (i.e., ± 200 Myr (2σ) or $<\pm 5\%$ over 4.5 Ga). Efforts are currently being made to synergize an instrument suite that can access the K-Ar decay system and reduce uncertainties through a more structured sample analysis campaign, but such an analytical sequence still requires multiple subsystems and demands a significant share of the mass and power resources allocated for a spacecraft (Cohen et al., 2014; Devismes et al., 2016; Farley et al., 2013).

Rb-Sr

In comparison to the other decay systems discussed, the Rb-Sr system can be (and has been) used to date igneous, metamorphic, and sedimentary materials, both terrestrial and extraterrestrial, via commercial instrumentation that maps to spaceflight-compatible technologies; thus, this radiometric system is highlighted for this study. ^{87}Rb decays to ^{87}Sr through beta-minus decay:



where β^{-} is a beta particle, ν_e is an electron antineutrino, and Q is the maximum decay energy. The decay constant (λ) of this reaction is $1.397 \cdot 10^{-11} \text{ yr}^{-1}$ equating to a half-life of $49.61 \cdot 10^9 \text{ yr}$ (Villa et al., 2015).

Like the other radiometric systems outlined above, variations in radiogenic ^{87}Sr are measured via isotopic ratios rather than absolute abundances, as ratios can be determined more precisely by mass spectrometry. When multiple cogenetic phases (e.g., minerals crystallized from the same melt) are analyzed, an isochron can be derived, defining the following linear relationship ($y = b + x \cdot m$):

$$^{87}\text{Sr}/^{86}\text{Sr}_{\text{measured}} = ^{87}\text{Sr}/^{86}\text{Sr}_{\text{initial}} + ^{87}\text{Rb}/^{86}\text{Sr}_{\text{measured}}(e^{\lambda t} - 1)$$

where ^{86}Sr , a stable isotope, is used to normalize isotopic abundances. The first term ($^{87}\text{Sr}/^{86}\text{Sr}_{\text{measured}}$) represents the modern day $^{87}\text{Sr}/^{86}\text{Sr}$ ratio measured directly in the sample, and the second term ($^{87}\text{Sr}/^{86}\text{Sr}_{\text{initial}}$) indicates the original $^{87}\text{Sr}/^{86}\text{Sr}$ ratio captured at the time of closure. The last term includes the modern day $^{87}\text{Rb}/^{86}\text{Sr}$ ratio measured directly from the sample, and the slope which uses the decay constant of ^{87}Rb (λ in yr^{-1}) to determine the age of the sample (t in yr). In most cases, $^{87}\text{Sr}/^{86}\text{Sr}_{\text{initial}}$ and t are not known for a given sample, so both are simultaneously solved for.

Both Rb and Sr are lithophile elements (i.e., affinity for silicate or oxide phases), incompatible during mantle melting (i.e., preferentially partition into the liquid relative to residual solid), and fluid soluble (i.e., mobilized by aqueous phases), leading to elevated concentrations of these elements in the terrestrial crust relative to the depleted mantle. Although their geochemical behaviors are similar, Rb is notably more incompatible and fluid soluble than Sr, leading to fractionation of Rb/Sr. Mantle-derived rocks, such as basalts and gabbros, have complementary low Rb/Sr ratios, challenging radiometric dating of mafic materials due to insufficient ^{87}Rb to produce measurable levels of radiogenic ^{87}Sr . Nonetheless, Rb-Sr ages are possible to calculate for mafic and ultramafic samples despite such limitations (see Walker et al., 1988).

Similar to measurements of K during K-Ar dating, in commercial and academic laboratories, Rb-Sr is traditionally analyzed by isotope dilution TIMS or multicollector ICPMS. However, recent technological advancements have made this

chronometer more accessible using Resonance Ionization Mass Spectrometry (Anderson et al., 2020) and ICPMS techniques (Farcy et al., 2020), both of which have the potential to enable *in situ* measurements for planetary applications with low uncertainties.

Mars as a Case Study

Martian history may be divided into four major eras, as shown in Figure 1; each of these eras is characterized by a specific mineralogy that predicated the presence and properties of water and/or liquid carbon dioxide during that period of time. In the terrains dating back to the early to mid-Noachian era (ca. 4.1 – ~3.9 Ga), there is an abundance of phyllosilicate minerals (such as chamosite and montmorillonite), suggesting a neutral to alkaline water-rich environment. In contrast, from the late Noachian to early Hesperian (ca. ~3.9 – ~3.4 Ga) there is an emergence of sulfate minerals (such as kieserite and gypsum), suggesting the transition to a water-limited acidic environment (Bibring et al., 2006). From the late Hesperian onwards (ca. 3.0 Ga to today) there is a dominance of anhydrous ferric oxides, which form in acidic, water-limited, oxidizing conditions. This mineralogical timeline indicates a shift in the mean pH level and availability of liquid water on the Martian surface (McSween and McLennan, 2005).

Mars does not exhibit obvious evidence of conventional plate tectonics, which are instrumental in enabling effective heat transfer from the deep interior and facilitating mixing between the mantle and crust on any given body. Without plate tectonics, the Martian crust and mantle reservoirs may have been cut off from each

other over geologic time scales. This may have resulted in mantle source regions remaining isolated.

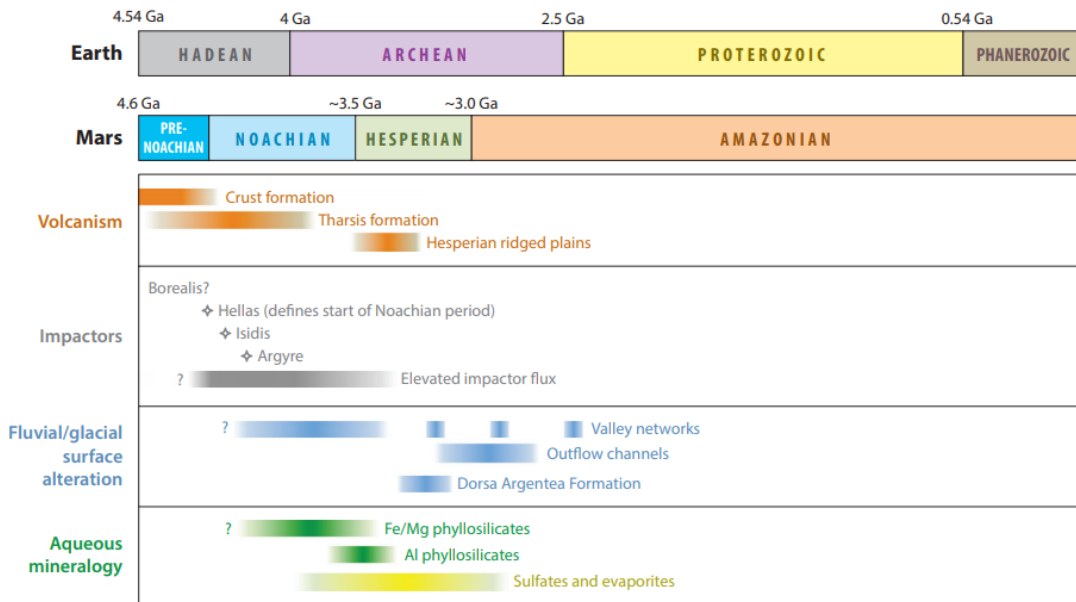


Figure 1 Timeline of major events in Martian history. While there is a lot of uncertainty around the absolute timing of these events, the sequence in which they occurred is known. The question marks indicate events that may have begun earlier but have a limited geologic record. From Wordsworth 2016.

Igneous activity on Mars has distributed basaltic flows across the upper crust of the planet. Consequently, weathering and erosion have produced a surface that is characterized mainly by sedimentary rocks and soils with basaltic compositions. These sedimentary rocks commonly contain pyroxene, olivine, plagioclase, and Fe-Ti oxides. Consequently, the Martian crust is more mafic than terrestrial continental crust. In fact, there is little evidence of siliceous igneous rocks based on global spectral surveys. While fractional crystallization is common in producing the diversity observed in the Martian crust, crustal rocks do not appear to remelt to form more silica-rich derivatives. A dacite flow in the Syrtis Major caldera, and some granitoid rocks in the central peaks of two craters near the caldera, are thought to be the sole examples of evolved igneous rocks on Mars (Christensen et al., 2005;

McSween and McLennan, 2005); however, the sources of these materials need further investigation.

The oldest terrains on Mars have varying percentages of Ca-rich pyroxenes, both with and without olivine grains present (Mustard et al., 2005). The proportion of low-Ca pyroxene decreases in younger terrains, potentially reflecting the depletion of water in the mantle as terrain formation continues (McSween et al., 2001, Poulet et al., 2009). Older terrains also have higher abundances of highly incompatible elements, such as radioactive K and Th, and lower abundances of Fe and fluid-mobile Cl compared to younger surfaces, possibly due to aqueous alteration.

The only samples of the Martian surface currently available for laboratory studies are select meteorites identified to be of Martian origin. While these rocks provide insight into their individual histories, studying these meteorites gives only a limited view into the thermal history of the planet from a global perspective. All of the Martian meteorites collected thus far have magmatic crystallization ages between 180 Ma and 1.3 Ga, likely reflecting their ejection from the surface via hypervelocity impacts from younger volcanic centers (McSween and McLennan, 2005). This introduces a sampling bias to studies of the Martian crust, limiting scientific understanding of what occurred to the last billion years on Mars. The absence of older samples highlights the necessity of either a sample return mission, as initiated by the Mars 2020 rover or a lander with *in situ* dating capabilities, to study terrains from the Noachian and Hesperian eras and find a link between the processes that occurred on the surface and the observed differences between the compositions of the surface and these meteorites.

A chronology-focused investigation sent to Mars could answer some of the questions raised around the *when*, *why*, and *how* of many of these processes. Such an investigation could help place quantitative constraints on when major geologic units were formed, calibrate the Martian crater record, explore the timings when potentially habitable hydrothermal regions existed, and date when tectonic processes may have been active, all primary objectives of the Planetary Decadal Survey (NRC, 2011).

Such a mission to Mars has the projected ability to answer the following questions:

- When and for how long was Mars wet and warm?
- For how long was Mars able to sustain the conditions under which biotic material could survive on the surface?
- How long can biotic material exist on a surface before being eradicated through erosion, cosmic ray exposure, and/or aqueous and other types of alteration (Cohen, 2020)?

There are many sites on Mars that could provide useful targets for a focused chronological study. Tharsis and Elysium, which are large hot spots on Mars, could provide information on the sources of current volcanism on the planet. Analyses at dendritic channels in the highlands could provide an estimate for when flowing water existed on Mars. Dating the dacite flow and the granitoid rocks near the Syrtis Major caldera could help explain how and when these siliceous rocks came to be on a planet dominated by basalts and devoid of archetypal plate tectonics. Constraining the ages of the hematite and jarosite deposits at Meridiani Planum, the volcanic rocks at Gusev Crater, and the carbonates at the Phoenix landing site would allow for constraints on the timing of the episodes when surficial liquid water was available (NRC, 2011).

Chapter 2: Methodology

Hardware

The analytical hardware used for this study was an Analyte G2 Excimer Laser Ablation system (193 nm wavelength) paired with a Nu AttoM sector field ICPMS instrument (Figure 2). The double-focusing Nu AttoM has a Nier-Johnson geometry that manipulates ion trajectories using an electrostatic analyzer that discriminates based on ion kinetic energy, followed by an electromagnet that affects mass-to-charge (m/z) ratio dependent curvature (Olesik, 2014). Sector field spectrometers such as this one operate by scanning at each chosen nominal mass station for a preselected amount of time.

During a typical analysis, the excimer laser system removes small amounts of sample mass through ablation via chemical and thermal mechanisms, which produces an aerosol composed of hot atoms, ions, molecules, and sub-micron particles that are entrained and transported into the ICPMS by way of a He carrier gas. Once the stream of particles from the ablation site is carried into the ICPMS, it interacts with a high temperature Ar plasma that serves to atomize and ionize the particles. The ionized material then passes through concentric sampler and skimmer cones, where the pressure lowers from atmospheric levels to between 10^{-4} - 10^{-6} Pa via differential pumping. A series of ion optics help to collimate and shape the beam to maximize ion transmission into the electrostatic analyzer and magnetic sector.

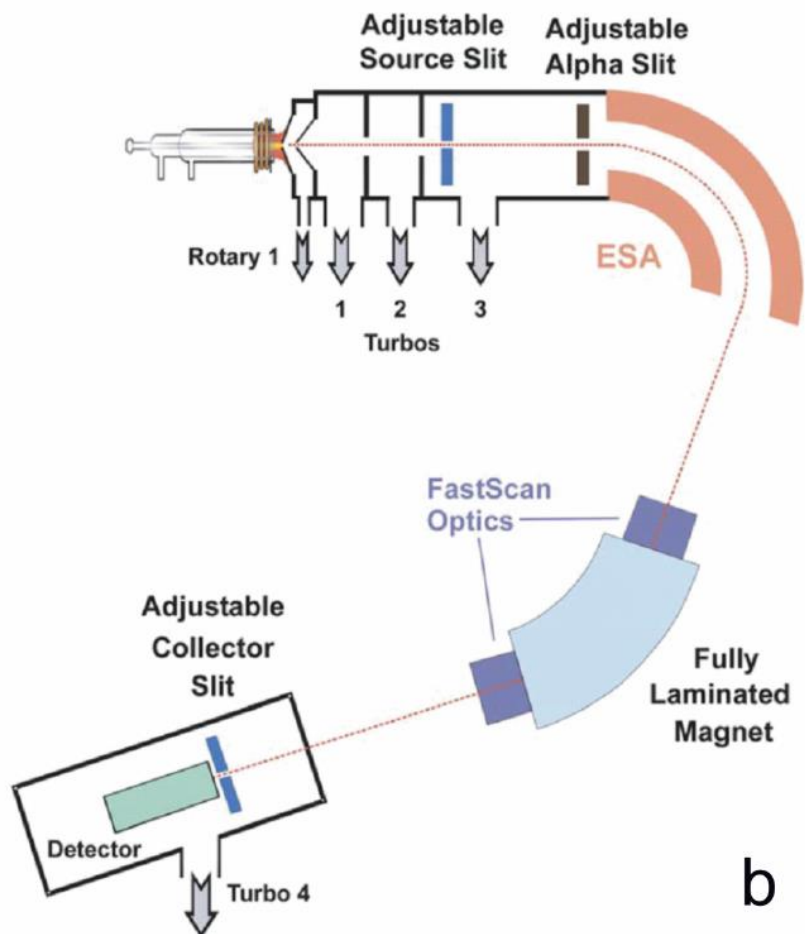


Figure 2 Schematic of a Nu AttoM setup. From Olesik, 2014.

The incoming ions are separated according to their respective mass-to-charge (m/z) ratios. However, the signal intensity at each mass station may include contributions from two or more isotopes and/or molecular ions, termed isobars, that have similar m/z ratios. Of particular importance for the Rb-Sr system are doubly charged rare earth elements (*e.g.*, $^{172}\text{Yb}^{2+}$ on mass $^{86}\text{Sr}^+$), diatomic oxides (*e.g.*, $^{70}\text{Zn}^{16}\text{O}^+$), argides (*e.g.*, $^{46}\text{Ca}^{40}\text{Ar}^+$), dimers (*e.g.*, $^{42}\text{Ca}^{44}\text{Ca}^+$), and atomic krypton (*e.g.*, ^{86}Kr) (see Table 1 for a more comprehensive list of isobaric interferences). Previous studies have shown that the production rates of doubly charged rare-earth elements, zinc oxides, and calcium dimers are sufficiently low and contribute only

minimally to Sr or Rb mass stations in basaltic materials (Arevalo et al., 2011; Cacopardo, 2020); recently, thorium oxide production rates were determined to be 1.3% with a 1300 W plasma on the Nu AttoM (Raith, 2021, pers. comm.). Other than Kr, which is sourced from the plasma gas thereby requiring correction, isobaric interferences are considered negligible for the sample set investigated here.

Table 1 Isobaric interferences in the mass range of interest.

Isotope	Abundance (%)	Isotopes (Interfering)	Oxides	Argides	Dimers	REE ²⁺
⁷⁷ Se ^a	7.63		⁶¹ Ni ¹⁶ O	³⁷ Cl ⁴⁰ Ar		¹⁵⁴ Sm ¹⁵⁴ Gd
⁷⁸ Se ^a	23.77	⁷⁸ Kr	⁶² Ni ¹⁶ O	³⁸ Ar ⁴⁰ Ar		¹⁵⁶ Gd ¹⁵⁶ Dy
⁸² Kr	11.58	⁸² Se	⁶⁶ Zn ¹⁶ O	⁴² Ca ⁴⁰ Ar		¹⁶⁴ Dy ¹⁶⁴ Er
⁸³ Kr	11.49		⁶⁷ Zn ¹⁶ O	⁴³ Ca ⁴⁰ Ar	⁴⁰ Ca ⁴³ Ca	¹⁶⁶ Er
⁸⁴ Sr	0.56	⁸⁴ Kr	⁶⁸ Zn ¹⁶ O	⁴⁴ Ca ⁴⁰ Ar	⁴⁰ Ca ⁴⁴ Ca	¹⁶⁸ Er ¹⁶⁸ Yb
⁸⁵ Rb	72.17		⁶⁹ Ga ¹⁶ O	⁴⁵ Sc ⁴⁰ Ar	⁴² Ca ⁴³ Ca	¹⁷⁰ Er ¹⁷⁰ Yb
⁸⁶ Sr	9.86	⁸⁶ Kr	⁷⁰ Zn ¹⁶ O ⁷⁰ Ga ¹⁶ O	⁴⁶ Ca ⁴⁰ Ar ⁴⁶ Ti ⁴⁰ Ar	⁴⁰ Ca ⁴⁶ Ca ⁴² Ca ⁴⁴ Ca ⁴³ Ca ₂	¹⁷² Yb
⁸⁷ Rb	7	⁸⁷ Sr	⁷¹ Ga ¹⁶ O	⁴⁷ Ti ⁴⁰ Ar	⁴³ Ca ⁴⁴ Ca	¹⁷⁴ Yb ¹⁷⁴ Hf
⁸⁸ Sr	82.58		⁷² Ge ¹⁶ O	⁴⁸ Ca ⁴⁰ Ar ⁴⁸ Ti ⁴⁰ Ar	⁴⁰ Ca ⁴⁸ Ca ⁴² Ca ⁴⁶ Ca ⁴⁴ Ca ₂	¹⁷⁶ Yb ¹⁷⁶ Lu ¹⁷⁶ Hf
⁸⁹ Y ^b	100		⁷³ Ge ¹⁶ O	⁴⁹ Ti ⁴⁰ Ar		¹⁷⁸ Hf

^a Se isotopes were included in the study to measure the interference posed on ⁸²Kr.

^b ⁸⁹Y was measured as a prospective internal standard to test the accuracy of measurements.

For the most precise isotopic measurements, deviations in the transmission efficiencies of ions with distinct m/z ratios need to be accounted for. This mass bias occurs because heavier ions are less easily deflected from the nominal ion path, a characteristic which fractionates the observed ratio of heavy-to-light ions from the

true composition of the sample (Maréchal et al., 1999; Albarede et al., 2004).

Quantitative treatment of the data are needed to correct this fractionation; Russell et al. (1978) proposed the following relationship to account for mass bias:

$$R_m = R_c * \left(\frac{m_1}{m_2}\right)^\alpha \quad \text{Equation 1}$$

where R_m is the ratio measured by the mass spectrometer, R_c is the correct (or empirically representative) ratio, $\frac{m_1}{m_2}$ is the ratio of the isotopic masses, and α is a calculated parameter that is constant between isotope pairs. The value for α may be derived by characterizing the observed fractionation between two isotopes whose abundances do not vary appreciably in natural systems (e.g., $^{88}\text{Sr}/^{86}\text{Sr}$), according to the following relationship:

$$\alpha = \frac{\ln\left(\frac{R_m}{R_t}\right)}{\ln\left(\frac{m_1}{m_2}\right)} \quad \text{Equation 2}$$

where R_t is the true (or natural) ratio.

Although this proposal focuses on accessing the Rb-Sr system via LA-ICPMS methods, other instruments may also hold the potential to provide *in situ* age measurements. For example, in academic laboratories TIMS is traditionally paired with isotope dilution to derive Rb-Sr ages; however, such instrumentation has not yet been developed for spaceflight, and wet chemical procedures are inherently risky and less conducive to autonomous operations. Resonance Ionization Mass Spectrometry is being explored as a means to provide coupled Rb-Sr and Pb-Pb age constraints by the CODEX (Chemistry, Organics, and Dating EXperiment) team, but this instrument requires multiple dedicated laser systems (Anderson et al., 2020), increasing power

and mass requirements. In comparison, LA-ICPMS enables streamlined analysis with hardware that has been or is currently being matured for spaceflight applications (*e.g.*, Farcy et al., 2020).

Analytical Techniques

Experiments were performed using the instrumental setup and tuning parameters of the ICPMS and laser ablation system detailed in Table 2. The beam size at the sample surface was typically 150 μm in diameter, but some felsic samples were ablated with an 85 μm beam to avoid detector saturation (*i.e.*, count rates above 3 million counts per second).

The gas flow rates and torch position were tuned daily to maximize the signal intensity at mass ^{175}Lu during the analysis of NIST 612 using an 85 μm spot size, 10 Hz repetition rate, and 5.1 J cm^{-2} fluence. Subsequently, each sample analysis comprised 60 to 240 s of ablation preceded by a background signal equal to 20% of the ablation time. Data were collected for ^{77}Se , ^{78}Se , ^{82}Kr , ^{83}Kr , ^{84}Sr , ^{85}Rb , ^{86}Sr , ^{87}Sr , ^{88}Sr , and ^{89}Y in “peak jump” mode. NIST 610 was chosen as the bracketing standard reference material to monitor instrumental drift.

Table 2 Operating conditions for the mass spectrometer and laser system tested in this study. Some of the parameters have multiple values listed; the parameters implemented are bolded.

Laser Parameters	Units	Value(s) Explored			
He carrier gas	L min ⁻¹	1			
Spot size	μm	85		150	
Repetition Rate	Hz	5	10		20
Fluence	J cm ⁻²	1.1	5.1		10.1
ICPMS					
RF Power	W	1000		1300	
Ar flow rate	L min ⁻¹	0.5			
Resolution	m/Δm	300			
Dwell Time	ms scan ⁻¹	0.2	0.5	2	5

Chapter 3: Results

Optimizing Analytical Parameters

All combinations of analytical parameters (Table 2) were run at both a radio frequency (RF) forward power of 1000 W and 1300 W. Plasmas maintained at lower RF powers are considered “cooler” and often used to reduce the production of doubly charged ions and select polyatomic ions (Fialho et al., 2011; Patterson et al., 1999; Fietzke et al., 2004). The capacity of the plasma to atomize larger particles and ionize elemental species with high first ionization energies is also at risk of being attenuated at reduced forward powers. Although a cool plasma was explored here in an attempt to limit spectral overlaps (*e.g.*, $^{172}\text{Yb}^{2+}$ on $^{86}\text{Sr}^{+}$), all measurements collected with a 1000 W plasma had negligible signal above background, indicating the limited atomization/ionization capabilities of the source. Thus, all the data reported here were collected with a “hot” plasma maintained at 1300 W forward power (Figure 3).

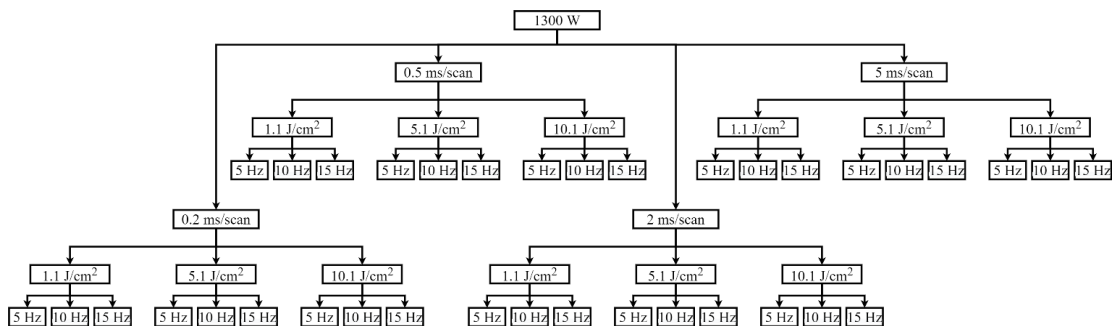


Figure 3 Range of configurations tested in the preliminary aspects of the study. The schematic only shows the configurations with an RF power of 1300 W; these are only half the configurations explored as an RF power of 1000 W was looked into as well.

Dwell time was another analytical variable that was explored in this study. This parameter is a measure of how long the mass spectrometer collects counts at each nominal mass station before transitioning to the next mass in the menu. Longer dwell times equate to more counts collected for each data point in a chromatogram (count rate versus time, see Figure 4 for an example) but slower scanning. The longer the dwell time, the more “lag” there is between the time when the first mass station is scanned and the last mass station in the menu is scanned. In comparison, shorter dwell times enable more rapid scanning and minimize “lag,” thereby allowing for a better characterization of sample heterogeneity on the micron scale by quickly returning to each mass station in an element menu. With this in mind, analyses were run at dwell times of 0.2 ms/scan (the fastest achievable scan rate of the Nu AttoM), 0.5 ms/scan, 2 ms/scan, and 5 ms/scan. As seen in Figure 5, shorter dwell times produced more precise $^{87}\text{Sr}/^{86}\text{Sr}$ measurements, indicating that faster scanning enables more reproducible signal collection. The analyses with longer dwell times have higher standard error of the means when compared to the 0.2 ms/scan dwell time runs.

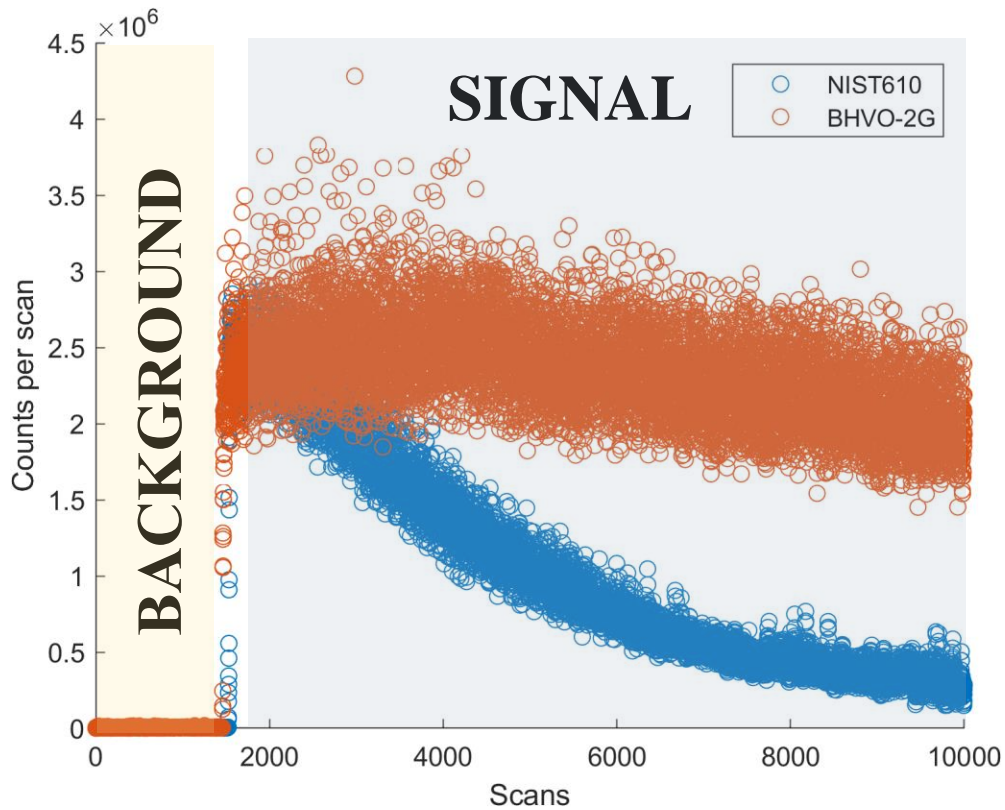


Figure 4 Sample chromatograms for NIST 610 and BHVO-2G at nominal mass station 88 showing the difference in signal intensity decay between the two samples. The first 1500 scans represent the background where the laser is firing but the shutter is closed (protecting the sample from the beam). There is a ramp up in signal from scans 1600-1650 as the laser starts to ablate the sample. From scan 1800 to the end is the signal from the sample; whereas the BHVO-2G signal exhibits only a limited decay (~20% decrease in signal intensity over 8000 scans), NIST 610 shows a much steeper decline (10x decrease in signal intensity over the same timeframe, possibly due to its optical properties).

The next parameter that was investigated was fluence, or the energy density of each laser shot. This study focused on fluences of 1.1 J/cm², 5.1 J/cm², and 10.1 J/cm², as such a range effectively captures the fluences achievable for a low power spaceflight laser system (*e.g.*, Fahey et al., 2020). Across all analyses, a fluence of 1.1 J/cm² yielded the highest standard error of the mean. The differences in the analyses that used higher fluences were less obvious, requiring that further analyses be carried out (see below).

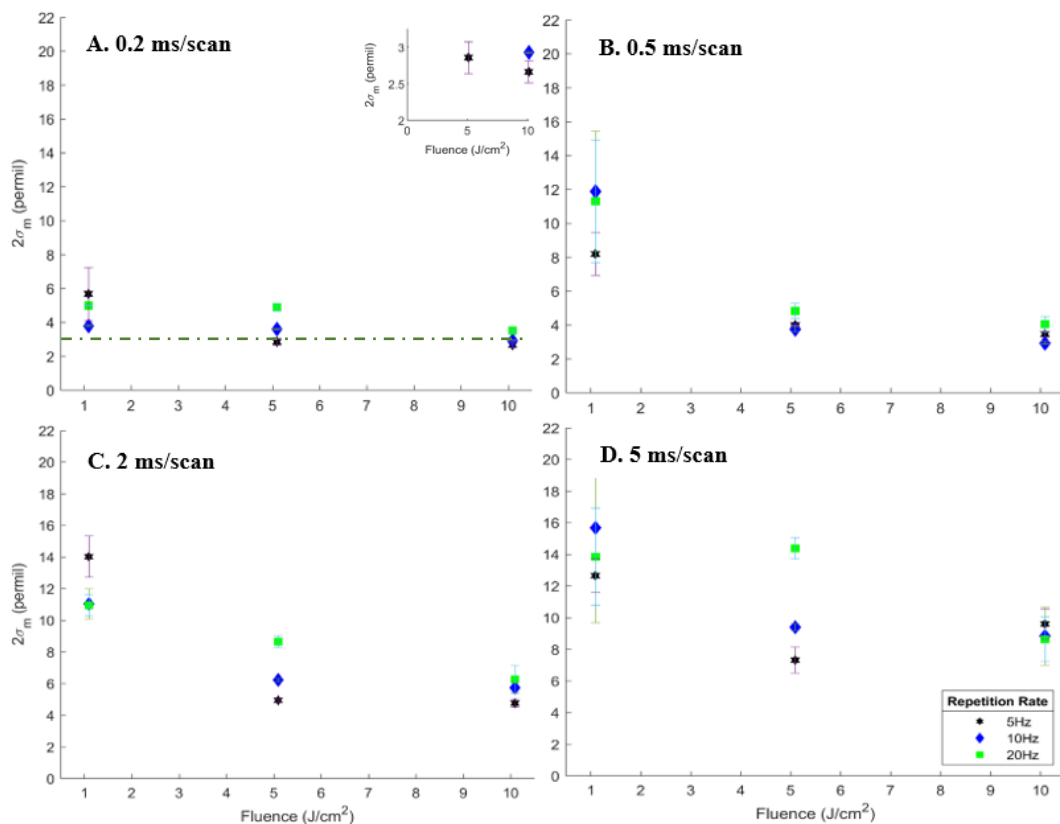


Figure 5 Precision vs fluence for configurations showing which combination of parameters yields the highest precision (i.e., the lowest $2\sigma_m$). Panels A-D represent different dwell times. Inset in A shows a magnified view of on all configurations with $2\sigma_m$ lower than 3 permil (below the green dashed line). Error bars are the standard deviation of the precision of three analyses per marker.

The last parameter explored in this study was the repetition rate, which is a count of the number of laser shots fired per second. Repetition rates of 5 Hz, 10 Hz, and 20 Hz were explored, with 20 Hz being the maximum repetition rate allowable for spaceflight solid-state laser ablation systems without active cooling (Fahey et al., 2020). The fastest repetition rate almost always yielded a less precise measurement of $^{87}\text{Sr}/^{86}\text{Sr}$, regardless of what the other parameters in that configuration were. One reason for this may be related to the analysis time; as the number of laser shots ($n = 1200$) was kept constant across all of these analyses in an attempt to control the depth (and by extension volume) of sample extracted per each analysis, the 20 Hz analyses

would have had the shortest analysis time, lasting a quarter of the time needed for the 5 Hz analyses. The short analysis time resulted in fewer completed scans for the highest repetition rate. Moreover, given a constant dwell time (and by extension scanning rate), shorter analyses result in a coarser characterization of the sample during depth profiling. For the two lower repetition rates, the precision was nearly the same, so further investigation was warranted.

Three ablations were completed on NIST 610 for each combination of parameters explored (listed in Table 2). The optimal parameters that had been identified previously (Figure 5) were a “hot” plasma power (1300 W) and a short dwell time (0.2 ms/scan). In order to further explore the ideal laser fluence and repetition rate, the analytical runs that yielded standard errors of the mean ($2\sigma_m$) lower than 3 permil were isolated (Figure 5 Inset). There were three such configurations:

1. Laser Fluence: 5.1 J/cm², Repetition Rate: 5 Hz
2. Laser Fluence: 10.1 J/cm², Repetition Rate: 5 Hz
3. Laser Fluence: 10.1 J/cm², Repetition Rate: 10 Hz

Each down-selected configuration was replicated nine times on NIST 610. After calculating $2\sigma_m$, the first configuration was chosen because it provided the most reproducible measure of internal precision (Figure 6). This configuration was used for the remainder of the study.

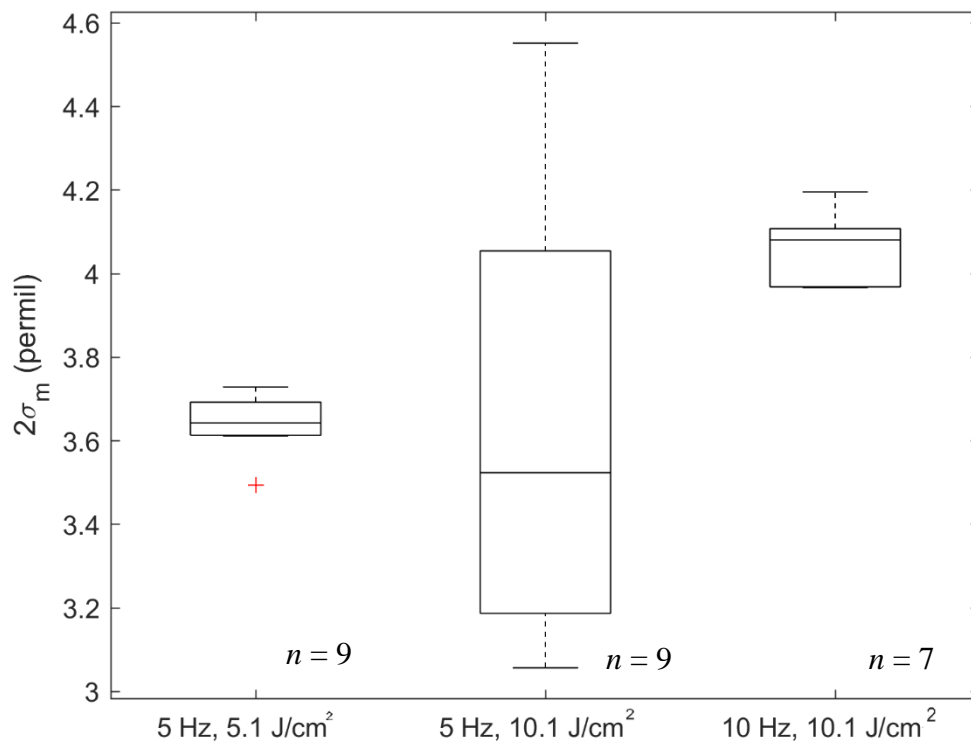


Figure 6 Standard error of the means of raw 87/86 ratios vs combinations of repetition rate and fluence to identify which configuration has the highest precision. All analyses were completed on NIST 610. The dwell time for these configurations is 0.2 ms/scan, and the RF power is 1300 W. The first configuration shows the most reproducible results.

The precision was calculated for each run based on the reproducibility of the ratio of the 87/86 mass station signals (without accounting for interferences) after an interquartile range (IQR) outlier rejection ($1.5 \cdot \text{IQR}$). Interestingly, the second configuration produced analytical runs with both the lowest and the highest precisions (Figure 6). The third configuration showed a smaller spread but had a higher $2\sigma_m$ (i.e. lower precision) than the other two configurations. Ultimately, the first configuration (1300 W forward power, 0.2 ms/scan dwell time, 5.1 J/cm² fluence, and 5 Hz rep rate) was determined to be optimal in terms of precision; all subsequent measurements were collected with these analytical conditions.

Data Preprocessing

In order to hone in on the bulk composition of the reference materials characterized here, data smoothing in the form of moving averages was considered as a way to attenuate fluctuations in signal intensities incurred by short wavelength anomalies (*e.g.*, shot-to-shot variations in laser energy, plasma flicker, electronic noise) rather than long wavelength trends (progressive 3D depth profiling of the sample). The application of a moving average as a smoothing function serves to reduce artificial noise.

Given the number of data reduction steps needed to derive $^{87}\text{Sr}/^{86}\text{Sr}$ ratios, there are multiple places where a moving average step can be added. For the purposes of this study, moving averages were investigated on either the raw signal at each nominal mass, or on the final $^{87}\text{Sr}/^{86}\text{Sr}$ ratios before outliers were rejected.

Regardless of where the smoothing was applied, the intervals were chosen to be 0, 2, 3, 4, 5, or 10, with 0 corresponding to no smoothing. The precision and accuracy of the final $^{87}\text{Sr}/^{86}\text{Sr}$ ratios were examined to evaluate the impact of each preprocessing regime, as seen in Figure 7. In general, averaging across a wider interval resulted in a monotonic improvement in precision. However, an apparent plateau/asymptote in accuracy was observed when incorporating moving averages; data smoothing improves the accuracy over unsmoothed data, but the interval over which it is smoothed has a negligible effect. Across all the reductions where the smoothing occurred at the final step, the precision and accuracy showed an increase much higher than the results of the reductions with smoothing of the raw data. Based on these observations, the smoothing step chosen for all analyses was applied on the

mass stations at the beginning of data reduction by intervals of 5 scans, as this was the more conservative choice of the two.

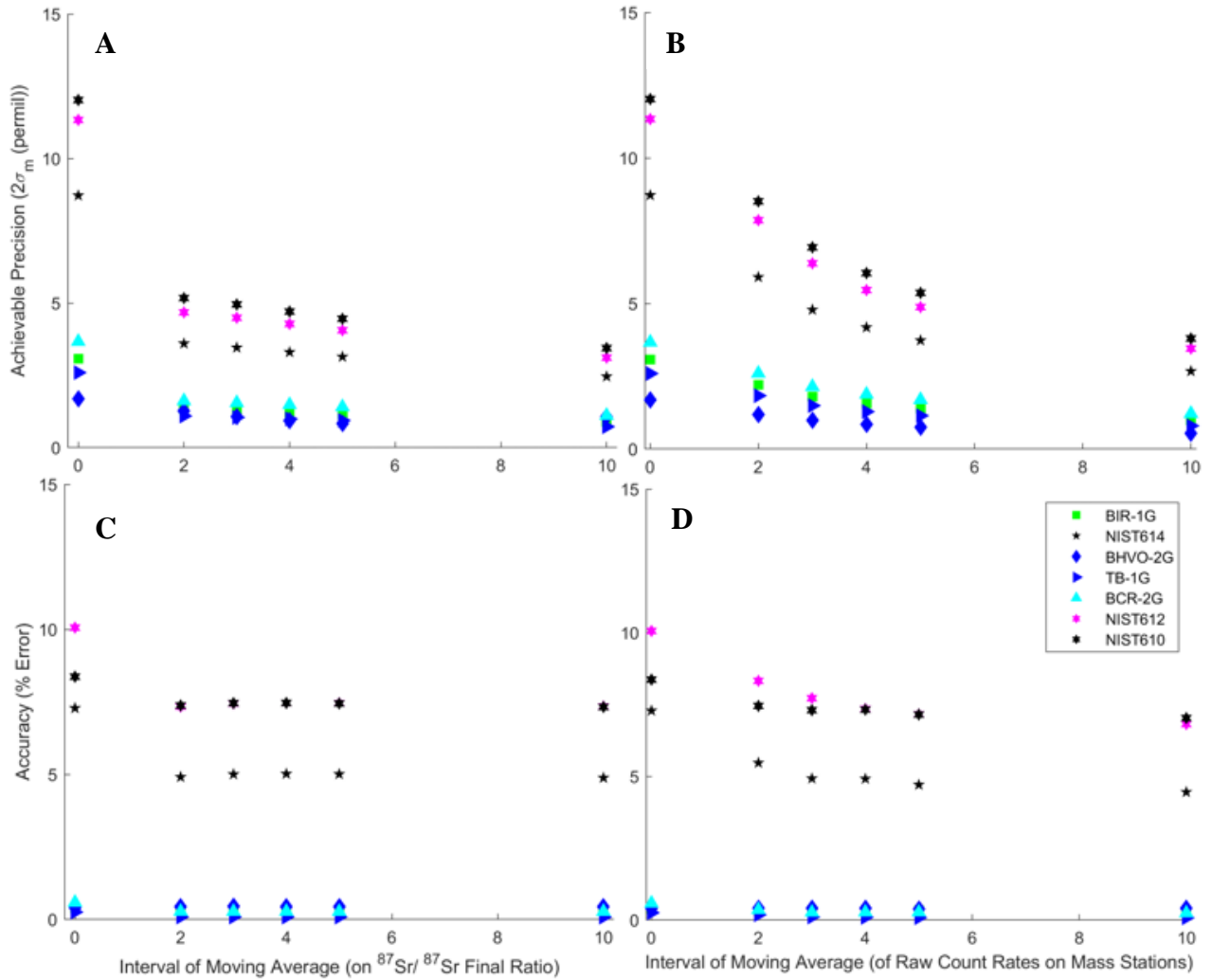


Figure 7 Scatter plots showing the effect of intervals of moving averages as a smoothing function on precision and accuracy. Panels A and B show the $2\sigma_m$ in permil for intervals over which the moving average is calculated. As the intervals increase, the precision increases with diminishing returns. Panels C and D show the % error for the intervals. The accuracy increases at an interval of 2 and then begins to plateau.

Data Processing

Masses 85 and 88 were assumed to only contain an isotope of Rb and Sr (*i.e.*, isobar-free, respectfully). Multiple Se mass stations were analyzed to determine if a Se correction to ^{82}Kr was needed; because ^{82}Se had a negligible effect on the results, the signal for this element was not used further. Thus, there was no need to correct for atomic isobaric interferences for the reference materials and basaltic samples investigated here.

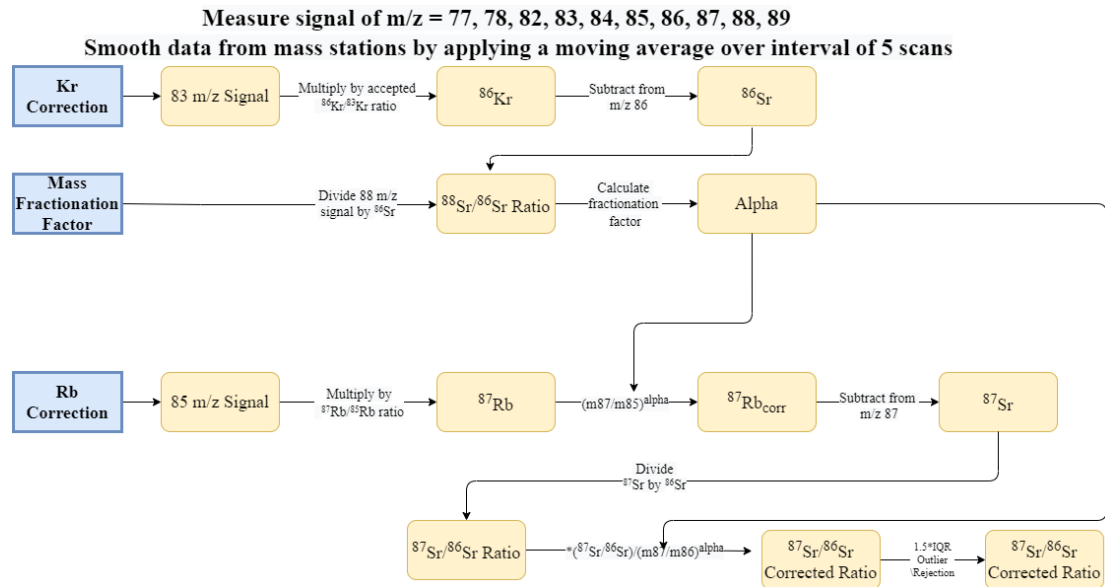


Figure 8 Flowchart showing the steps taken to calculate $^{87}\text{Sr}/^{86}\text{Sr}$ ratios.

Canonical isotope ratios, such as those used in the data processing techniques described further below (e.g., $^{88}\text{Sr}/^{86}\text{Sr}$), are invariable in nature due to the relatively homogeneous distribution of these nucleosynthetic constituents in the solar nebula. However, ratios that incorporate a radiogenic isotope (e.g., $^{87}\text{Sr}/^{86}\text{Sr}$) reflect nucleosynthetic contributions as well as accumulated products of radioactive

decay. All canonical ratios used in the reduction scheme were derived from Rosman and Taylor (1999).

The raw data from each analysis (count rates versus time) were exported to Excel for data processing and then a moving average was applied over an interval of 5 scans. The first step in determining the $^{87}\text{Sr}/^{86}\text{Sr}$ ratio of each calibrant or sample involved separating isobaric Kr and Sr signals on mass 86. More specifically, measured count rates of ^{83}Kr were multiplied by the canonical $^{83}\text{Kr}/^{86}\text{Kr}$ ratio to calculate ^{86}Kr , which was then subtracted from the signal measured at mass station 86 in order to isolate the contribution of ^{86}Sr , as shown in Figure 8. The ^{86}Sr signal was used to calculate the measured background subtracted $^{88}\text{Sr}/^{86}\text{Sr}$ ratio, which was levied along with the canonical $^{88}\text{Sr}/^{86}\text{Sr}$ ratio to calculate the fractionation factor α in Equation 1.

The ^{85}Rb signal was multiplied by the canonical $^{87}\text{Rb}/^{85}\text{Rb}$ ratio to yield the ^{87}Rb signal, and a mass correction was applied using the α factor described above and Equations 1 and 2, which allowed for the isolation of the ^{87}Sr signal. This signal is divided by the calculated ^{86}Sr signal to yield the measured $^{87}\text{Sr}/^{86}\text{Sr}$ ratio. A mass fractionation correction was applied to this ratio using the α factor calculated earlier and Equation 2. An outlier rejection based on 1.5 times the interquartile range was applied at the very end.

Another complication to consider is elemental fractionation, in which elements are atomized/ionized with varying degrees of efficiency depending on factors such as condensation temperature (and volatility by extension), period, group, and atomic number. Rb and Sr tend to fractionate differently from each other, with Sr

displaying a progressive decrease in signal over the course of an ablation and Rb remaining at a relatively constant signal, according to a study by Jenner and O'Neill (2012). The data presented here corroborates this phenomenon, with the Rb/Sr ratio increasing slightly from the beginning to the end of an analysis. However, elemental fractionation (by definition) does not affect isotope ratios of the same element, so we do not need to consider the effects of elemental fractionation on our $^{87}\text{Sr}/^{86}\text{Sr}$ ratios. Similarly, our calculation of ^{87}Rb from ^{85}Rb using the canonical $^{87}\text{Rb}/^{85}\text{Rb}$ ratio is also unaffected by elemental fractionation. No elemental fractionation correction is applied to any of the data presented.

As the method presented depends on corrections based on nominal mass stations that are isobar-free (^{83}Kr and ^{85}Rb), analytical uncertainties on those mass stations are carried over to the subsequent steps in the data reduction scheme. For example, if the signal on ^{85}Rb is inaccurate (due to insufficient characterization of isobaric interferences, high artificial background, *etc.*), this inaccuracy would propagate onto ^{87}Rb , ^{87}Sr and, by extension, the final $^{87}\text{Sr}/^{86}\text{Sr}$ ratios.

Accuracy and Precision

The accuracy of the analyses for each sample, based on the corrections and reduction steps listed above, may be dependent on the silica content of the sample. In the sample set explored here, the basaltic samples yielded the most accurate and precise $^{87}\text{Sr}/^{86}\text{Sr}$ ratios. The range of precisions were between 0.8 permil (BHVO-2G, $2\sigma_m$) to 1.4 permil (BCR-2G, $2\sigma_m$). The $^{87}\text{Sr}/^{86}\text{Sr}$ ratios of the basaltic samples deviated from the accepted values from $\pm 0.16\%$ (TB-1G) to $\pm 0.47\%$ (BCR-2G).

The accuracies for the synthetic NIST samples need further discussion. The chromatograms of the NIST samples display a rapid decay in signal intensity. Some signal decline is expected as an analysis continues. With each successive shot, the laser removes less material, creating a tunneling effect where the radius at the bottom of an ablation crater is smaller than at the sample surface; as less material is ablated, fewer counts are detected. However, the chromatograms of the NIST samples show a much faster decay than those observed in the signals of the basalt samples (*e.g.*, Figure 4). The NIST 610 analyses show that the signal intensity decreases by over an order of magnitude over the duration of the analysis.

NIST 610 and NIST 612 produced the most inaccurate $^{87}\text{Sr}/^{86}\text{Sr}$ ratios (see Figure 9), whereas NIST 614 provided the most accurate ratio of the NIST reference materials. This was unexpected as NIST 614 is the thinnest sample optically (*i.e.* allows light to pass through most easily). Optically transparent materials may allow the laser to remove more material than an optically opaque material would. As the laser continues interacting with the material, the aspect ratio of the ablation pit decreases, and less material is ablated with each successive laser shot. The transparent material enhances this effect, as more material is ablated initially and a tunneling effect occurs much sooner than with translucent or opaque samples. This hypothesis may explain why NIST samples exhibit a decay in their signal intensity as an analysis continues and why their $^{87}\text{Sr}/^{86}\text{Sr}$ ratios are inaccurate relative to the basalt samples. Given that NIST 610 provided the least precise and least accurate data, it is prudent to report its numbers as the lower threshold for the two metrics; the precision identified

for NIST 610 is 4.4 per mil ($2\sigma_m$) and the accuracy is $\pm 7.5\%$ deviation from the accepted values.

As for the Rb/Sr ratios, $^{85}\text{Rb}/^{88}\text{Sr}$ was used as a proxy to determine the accuracy and precision metric as these two mass stations do not have significant isobaric interferences. The average background corrected signal for mass station 85 was divided by the average background corrected signal for mass station 88. Figure 10 shows the $^{85}\text{Rb}/^{88}\text{Sr}$ ratios (normalized to the accepted values), with the samples with the lowest Rb/Sr ratios (BIR-1G and NIST 614, with ratios of 0.0018 and 0.018, respectively) demonstrating $^{85}\text{Rb}/^{88}\text{Sr}$ ratios with up to an 80% deviation from the accepted ratio. These samples are heavily depleted in both Rb and Sr, and any elemental fractionation at such low Rb/Sr ratios would yield an increase of the measured ratio. The $^{85}\text{Rb}/^{88}\text{Sr}$ ratios for these two samples were treated as outliers as any deviation from the accepted ratio at that order of magnitude would result in a more inaccurate ratio than for the other samples.

The rest of the samples exhibit accuracies ranging from a $\pm 0.2\%$ deviation (NIST 612) to a $\pm 13\%$ deviation (BCR-2G) from the accepted values. An average accuracy of $\pm 9\%$ deviation is assumed for Rb/Sr ratios for the remainder of this study.

The precision of the $^{85}\text{Rb}/^{88}\text{Sr}$ ratios was distributed between 21 permil (NIST610, $2\sigma_m$) and 490 permil (BIR-1G, $2\sigma_m$). NIST 614 had a standard deviation of 230 permil ($2\sigma_m$). As before, BIR-1G and NIST 614 were treated as outliers given their level of depletion in Rb and Sr, their low Rb/Sr ratios, and their imprecise (and inaccurate) $^{85}\text{Rb}/^{88}\text{Sr}$ ratios. After removing these two samples from the set, the least precise measurement was for TB-1G (7.8 permil, $2\sigma_m$). Taking the average of these

values yielded a precision of 5%; this value was used as the precision metric for $^{85}\text{Rb}/^{88}\text{Sr}$ ratios in the remainder of the study.

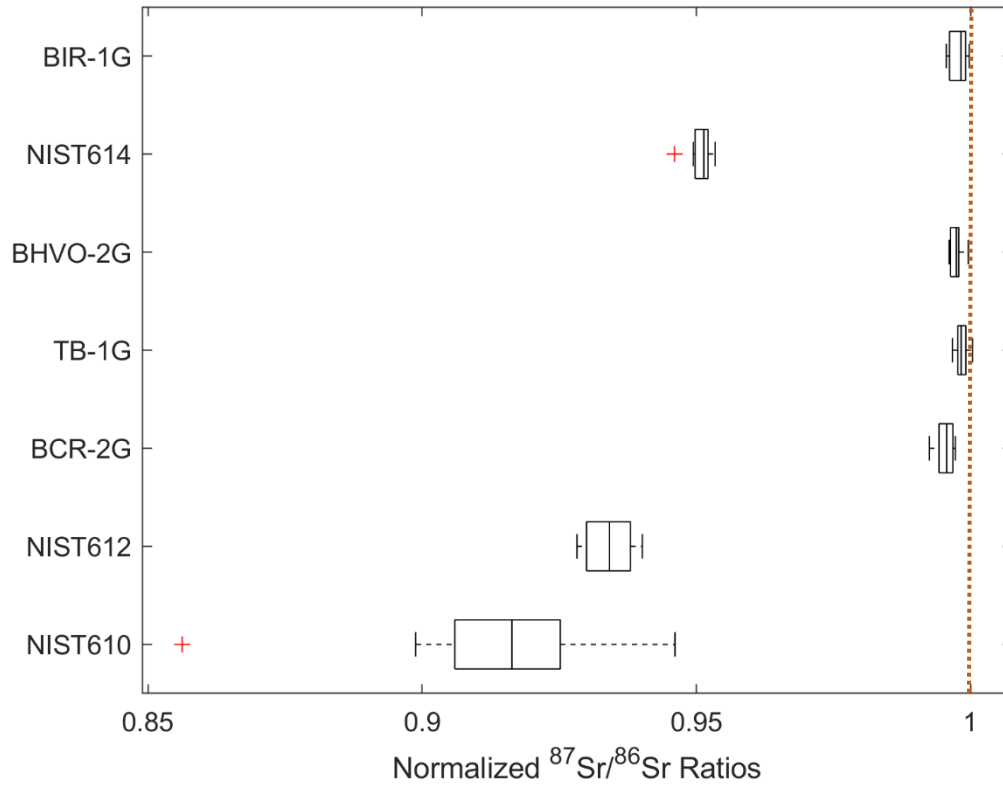


Figure 9 Normalized $^{87}\text{Sr}/^{86}\text{Sr}$ ratios for nine replicates for each sample show that the basalt samples analyzed have a higher accuracy than the NIST samples when compared to the accepted values. NIST 610 and NIST 612 in particular display a range in $^{87}\text{Sr}/^{86}\text{Sr}$ ratios. All measurements are systematically lower than the expected ratios.

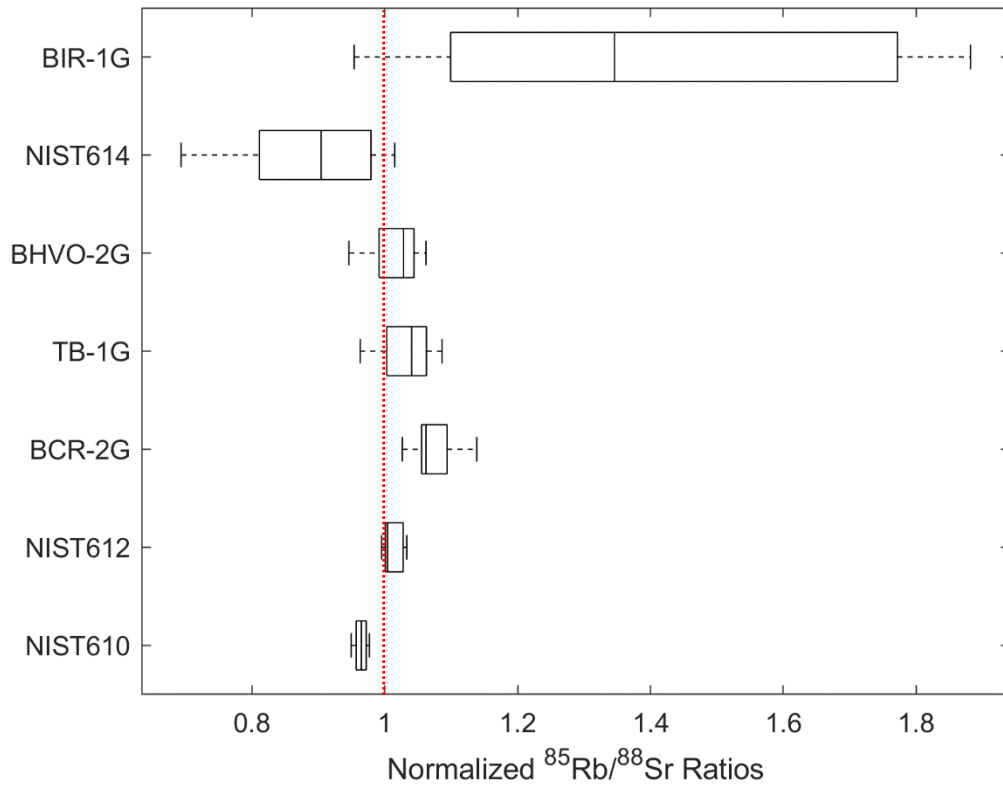


Figure 10 Normalized ⁸⁵Rb/⁸⁸Sr ratios for nine replicates for each sample show that while most of the samples display accurate ⁸⁵Rb/⁸⁸Sr ratios with less than 13% deviation from the accepted ratio, the samples with the lowest Rb/Sr ratios (BIR-1G and NIST 614) exhibit a wider range of ratios.

Chapter 4: Discussion and Conclusions

Extrapolating to Higher $^{87}\text{Rb}/^{86}\text{Sr}$ Ratios

The compositions of the reference materials investigated here extend over only a limited range in $^{87}\text{Rb}/^{86}\text{Sr}$; the highest $^{87}\text{Rb}/^{86}\text{Sr}$ ratio for which analyses were completed is for NIST 610, with a value of 2.3. Although felsic minerals may extend to significantly higher $^{87}\text{Rb}/^{86}\text{Sr}$ (*e.g.*, biotite can have a $^{87}\text{Rb}/^{86}\text{Sr}$ ratio of up to 350 (GEOROC, 2021)), most of the reference materials analyzed here may be classified as basaltic in composition, with the exception of the NIST glasses. Because the lithologies found on Mars may be defined by a greater variance in Rb/Sr, a model is proposed to estimate the standard error of the means of $^{87}\text{Sr}/^{86}\text{Sr}$ in materials with $^{87}\text{Rb}/^{86}\text{Sr}$ ratios beyond those investigated empirically through this study.

The measured $^{87}\text{Sr}/^{86}\text{Sr}$ ratios for the samples analyzed were used to extrapolate to higher $^{87}\text{Rb}/^{86}\text{Sr}$ ratios (GeoReM, 2021). A bivariate ordinary least squares linear regression was used to assess this dataset with the $^{87}\text{Rb}/^{86}\text{Sr}$ ratio as the independent variable and the standard error of the mean of the $^{87}\text{Sr}/^{86}\text{Sr}$ ratio as the dependent value (Figure 11), as informed by the data collected in this study. For the purposes of this regression, the independent variable was defined as the accepted values in lieu of the measured values; the uncertainty on the $^{87}\text{Rb}/^{86}\text{Sr}$ ratio is considered negligible as they are very low compared to the ratios in question.

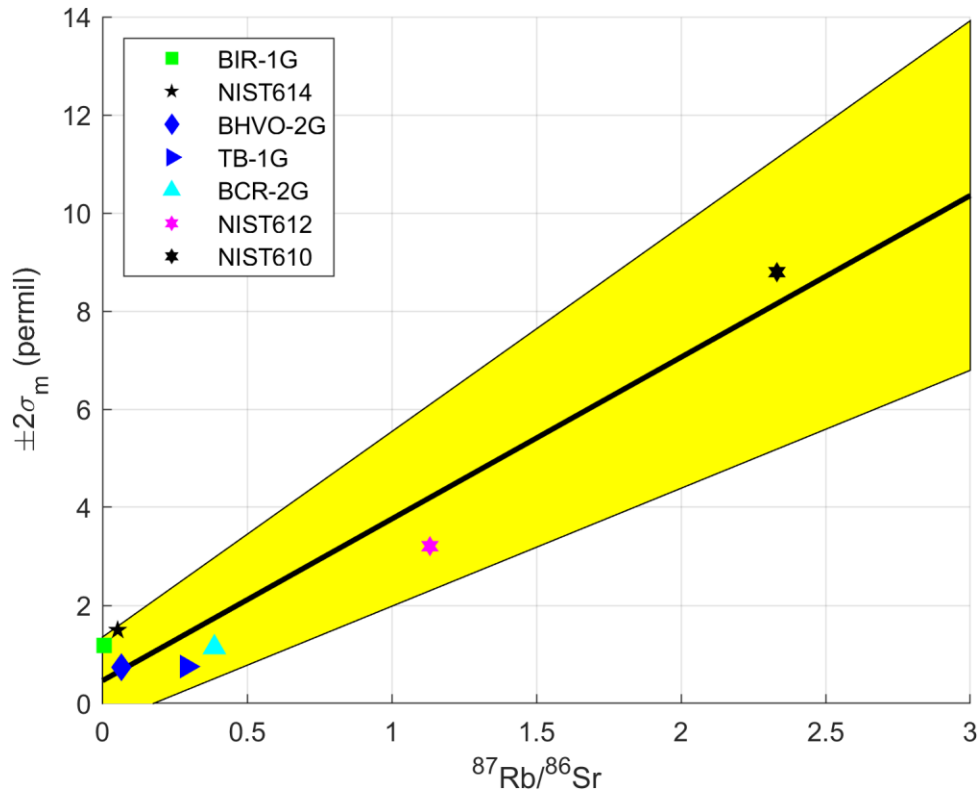


Figure 11 The standard error of the means for the $^{87}\text{Sr}/^{86}\text{Sr}$ ratios of the samples analyzed regressed against the accepted $^{87}\text{Rb}/^{86}\text{Sr}$ ratios to extrapolate to higher $^{87}\text{Rb}/^{86}\text{Sr}$ ratios. A bivariate linear regression was completed to determine the line of best fit (thick black line) and the error envelope for this line (yellow). Legend is arranged from lowest (BIR-1G) to highest $^{87}\text{Rb}/^{86}\text{Sr}$ ratio (NIST 610).

Poisson counting statistics were considered for each sample as an alternate measure of precision for the $^{87}\text{Sr}/^{86}\text{Sr}$ and the $^{87}\text{Rb}/^{86}\text{Sr}$ ratios. Assuming a maximum count rate of 3 million counts per second (the threshold before the instrument attenuates the signal to protect the electron multiplier) over 8000 scans for 2 ms/scan, the maximum number of counts in any single analysis is 48 million counts. After separating these counts into counts of ^{87}Rb and ^{87}Sr based on the Rb/Sr ratio of each sample, the Poisson counting standard deviation ($\frac{1}{\sqrt{N}}$, where N is the number of counts) was calculated. For both ^{87}Rb and ^{87}Sr , the precision based on Poisson counting statistics was up to two orders of magnitude lower than the precision identified earlier for each variable (determined by the linear regression shown in

Figure 11 for $^{87}\text{Sr}/^{86}\text{Sr}$ ratio and capped at 5% of the ratio for $^{87}\text{Rb}/^{86}\text{Sr}$). The latter was chosen as the metric of use for the remainder of this study as it represents more conservative values.

Synthetic Isochron

A natural isochron relies on measuring ratios of the radioactive (parent) isotope and the radiogenic (daughter) isotope, both normalized to a non-radiogenic isotope of the daughter element. The minerals analyzed for an isochron need to be cogenetic, defined as having been crystallized from the same melt with identical initial isotopic compositions at the time of crystallization. As no individual minerals were analyzed in this study, a synthetic isochron with randomly generated $^{87}\text{Rb}/^{86}\text{Sr}$ was developed to explore the accuracy and precision of inferred ages using this method.

A Monte Carlo simulation created in Matlab was used to produce the data for a suite of synthetic isochrons. To create each independent synthetic isochron, either 2, 5, 10, 15, 20, 50, or 100 $^{87}\text{Rb}/^{86}\text{Sr}$ ratios were generated using a random number generator with a normal distribution between the ranges 0 and 30.0; the number of data points varies between the minimum number needed to define a line (2) to a large number of data points (50 or 100, depending on how long each analysis takes and how much of the sample is available). The range in $^{87}\text{Rb}/^{86}\text{Sr}$ represents those that could be expected during the analysis of minerals with very little Rb (such as plagioclase) to the lower end of the Rb-range seen in micas; these ranges of $^{87}\text{Rb}/^{86}\text{Sr}$

were derived from mineral data downloaded from GEOROC (2021), which were averaged after a $1.5 \times \text{IQR}$ outlier rejection.

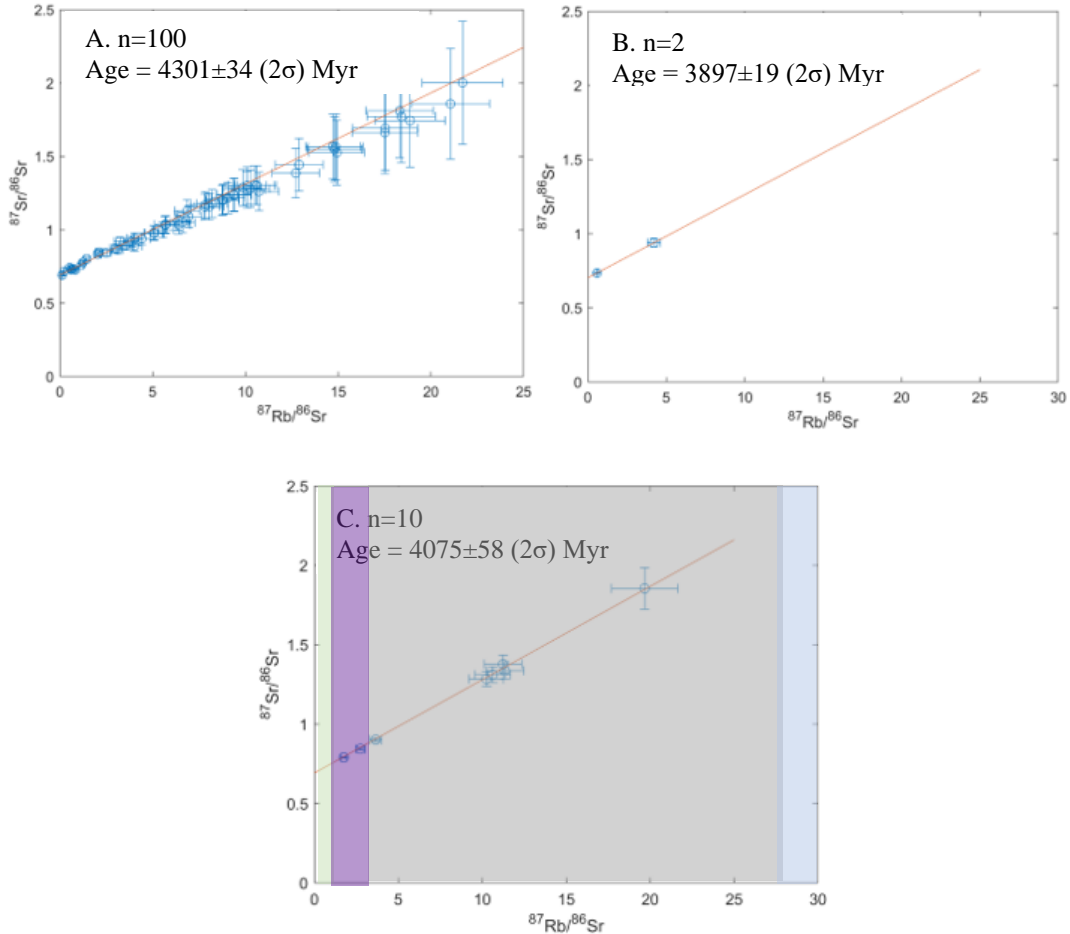


Figure 12 Examples of synthetic isochrons with various number of data points and the resulting precision and accuracy of the inferred age. Panel A shows an isochron with 100 data points that has an inaccurate but precise age. Panel B shows one of the few isochrons with 2 data points that yields a precise age. Panel C is an example of an accurate and a precise age. The colors show the ranges in $^{87}\text{Rb}/^{86}\text{Sr}$ ratios for four minerals: plagioclase (light green), hornblende (purple), potassium feldspar (grey), and muscovite (light blue) (Data from GEOROC).

At any given $^{87}\text{Rb}/^{86}\text{Sr}$ ratio, the $^{87}\text{Sr}/^{86}\text{Sr}$ ratio that plots along a 4.0 Ga isochron was derived. A 5% standard error of the mean and a $\pm 9\%$ deviation from accepted value were assumed for the $^{87}\text{Rb}/^{86}\text{Sr}$ ratios as they were the achievable metrics identified earlier. For the $^{87}\text{Sr}/^{86}\text{Sr}$ ratios, the calculated ratios for the basaltic

samples only deviated from the accepted ratios by under 0.38% in terms of accuracy. As such, an accuracy of $\pm 0.5\%$ from true was assumed for all $^{87}\text{Sr}/^{86}\text{Sr}$ ratios; a randomly generated number between 0 and 1 was multiplied by this metric and added to all generated ratios as noise to simulate analytical uncertainty. The precision of the $^{87}\text{Sr}/^{86}\text{Sr}$ ratios was determined for all generated data points based on the regression relationship established earlier (Figure 11).

Thirty synthetic isochrons were generated for each sample size per run; each suite of isochrons (*i.e.*, 2, 5, 10, 15, 20, 50, or 100 data points) was used to create a robust dataset that can be used to determine model ages and evaluate performance statistics. A York linear regression was performed on the data points of each isochron (Figure 12) to identify the slope of the best fit line, enabling the calculation of an inferred age. This specific regression type was deemed most appropriate as it accounts for uncertainties in both the x and the y values by weight and minimizes residuals orthogonal to the best fit line. A $1.5 \times \text{IQR}$ outlier rejection was applied.

The synthetic isochrons that incorporated just two data points were found to be insufficient to meet the precision benchmark targeted by the Technology Roadmap (Figure 13). As more data points were considered, the uncertainty on the inferred age decreased. Based on the 2σ uncertainty of the ages calculated using the figures of merit defined throughout this study, a minimum of 10 data points are needed to definitively generate an isochron that meets the goal of a precision within ± 200 Myr.

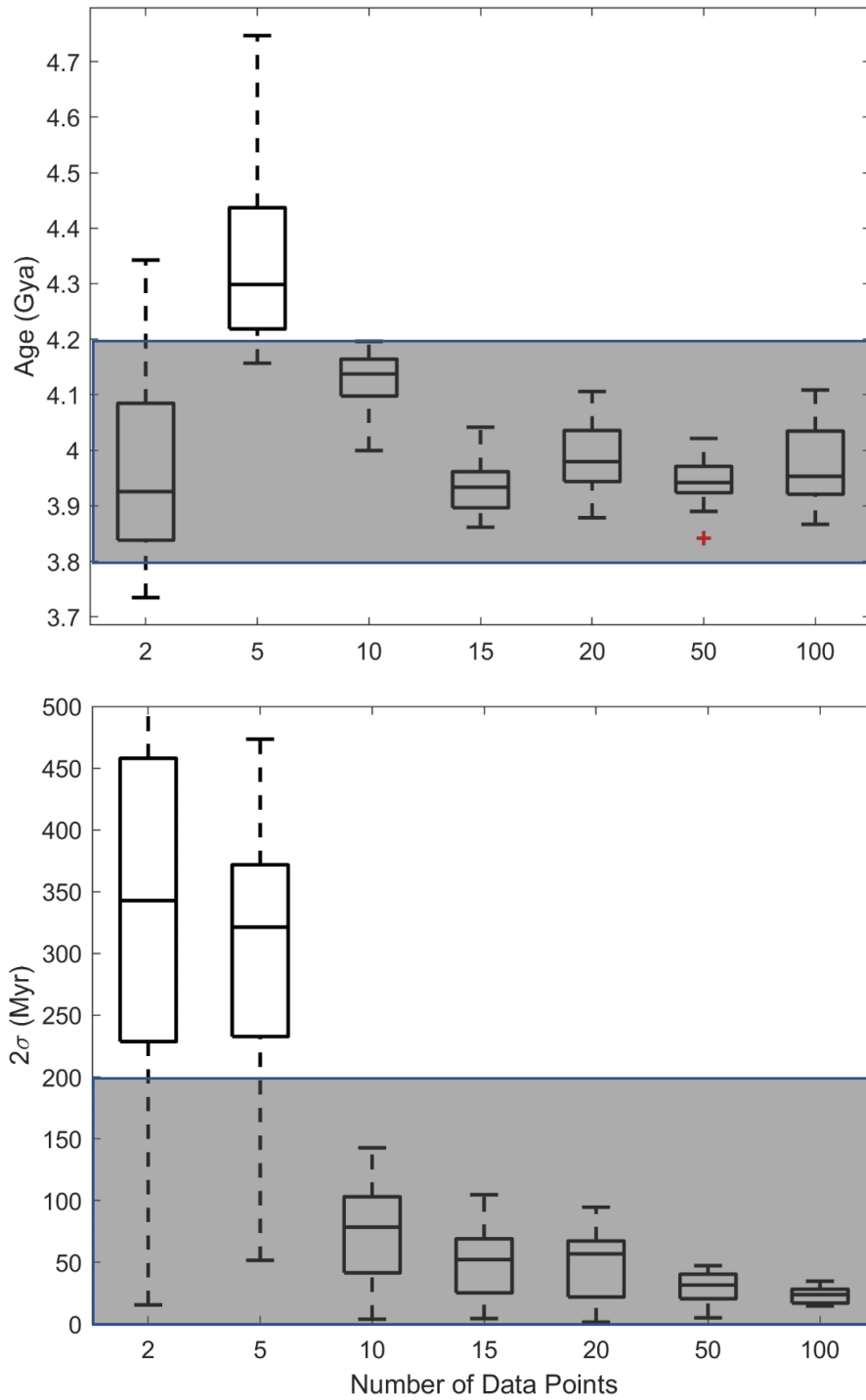


Figure 13 Comparison of precision and accuracy of inferred ages based on the number of data points collected from one run of the Monte Carlo simulation which produces 30 isochrons. The top panel shows how accurate the ages are from the 30 isochrons generated for different number of data points used. There does not seem to be a correlation between the number of data points used and the accuracy of the age. The bottom panel shows how well these ages met the precision benchmark set by the NASA Roadmap. As the number of data points included in the model increases, the age measurements become more precise. The inset shows the wide range of uncertainties given 2 data points.

Although more sample analyses (data points) yield higher precision age estimates, the accuracy does not follow the same trend. Figure 13b shows a lack of correlation between the number of data points used in generating an isochron and the accuracy of the inferred age of the sample. Interestingly, the randomization function built into the Monte Carlo simulation affects the accuracy of ages inferred from 10 and 15 data points; 8 out of 10 repetitions of the simulation yielded ages within the grey area in Figure 13b. Given this complication, a conservative suggestion of using at least 20 data points is supported for accurate inferred ages. If more of the generated data points are clustered at higher $^{87}\text{Rb}/^{86}\text{Sr}$ ratios, the 9% accuracy on the $^{87}\text{Rb}/^{86}\text{Sr}$ would skew the line of best fit accordingly; a study investigating the spacing of the data points within the range of $^{87}\text{Rb}/^{86}\text{Sr}$ in this model may be of merit.

Conclusions

Determining the age of surfaces of rocky planetary bodies *in situ* within the framework set by the NASA Technology Roadmap requires instrumentation capable of measuring accurate and precise ages. The LA-ICPMS technique is suggested a viable candidate for a planetary chronology mission and shown to yield Rb-Sr ages within the precision benchmark set by the NASA Technology Roadmap, specifically ± 200 Myr (2σ) on a 4 Gyr sample. A minimum of 10 sample analyses is recommended to meet these metrics.

The results of this study show that LA-ICPMS can be a useful technique for *in situ* planetary chronology and highlight the need to put effort into the maturation of an instrument capable of reproducing the methods demonstrated here.

Future Work

The work completed has revealed complexities in the method, from data collection to statistical treatments. Attempts were made to explore the trade space of these complexities, but there are many ways in which this study could be expanded. The following are a few ways identified that are immediately possible to investigate given that all the instrumentation needed is available:

- Analyze samples across a wider range of compositions
 - Ablate samples with higher $^{87}\text{Rb}/^{86}\text{Sr}$ ratios: the sample with the highest $^{87}\text{Rb}/^{86}\text{Sr}$ ratio measured thus far was NIST 610, which has a ratio of 2.3. The uncertainty in $^{87}\text{Sr}/^{86}\text{Sr}$ is shown to increase with higher $^{87}\text{Rb}/^{86}\text{Sr}$ ratios, as seen in Figure 9; more analytical data points will allow for a more comprehensive investigation into the relationship between the two variables and inform on whether this relationship is a linear one or one that plateaus past a certain $^{87}\text{Rb}/^{86}\text{Sr}$ ratio; such an addition to the study would convert projections to empirical constraints.
 - Ablate natural samples: all the samples studied here were homogenized glasses. Models have been used to generate data points that mimic cogenetic minerals. Exchanging these models for an isochron based on mineral data from a sample previously analyzed by a ground-truth technique (*e.g.*, isotope dilution and multicollector ICPMS) will allow for a higher fidelity answer to the question of whether or not this method satisfies the NASA Roadmap's

constraints. For an extension of this nature, samples such as granites, basalts, and Martian meteorites (if available) are recommended.

Sedimentary samples could also prove useful, if more complicated to analyze.

- Constrain isobaric interferences from oxides, argides, dimers, and doubly charged rare earth elements during the analysis of more felsic samples: the accuracy of the $^{87}\text{Sr}/^{86}\text{Sr}$ in the samples analyzed thus far suggests that isobaric interferences are negligible during the analysis of basaltic reference materials. A more complete investigation into the production rates of these interferences in more silica-rich lithologies would allow for a subtraction of the interference, allowing for only the signal from the isotopes of interest to be included in the data treatment.
- Investigate the rapid signal decay for the NIST samples: the decay of the signal intensities of the NIST samples may be due to the optical properties of the standards. A thorough test of this hypothesis could inform on the shortcomings of study when investigating transparent or translucent minerals.

Appendix A

Seven spreadsheets are attached, separated by sample name. The table below shows the order in which analyses were completed. The sheet name in the excel spreadsheets indicate the analysis number. For all analyses, unless otherwise noted, the spot size was 150 microns; the other parameters were held constant throughout this experiment.

Analysis Number	Sample	Repetition	Note
3462	NIST 610	1	
3463	NIST 610	2	
3464	NIST 610	3	
3465	NIST 610	4	
3467	BHVO-2G	1	
3468	BHVO-2G	2	
3469	BHVO-2G	3	
3470	BHVO-2G	4	
3471	BHVO-2G	5	
3472	BHVO-2G	6	
3473	BHVO-2G	7	
3474	BHVO-2G	8	
3475	BHVO-2G	9	
3476	NIST 610	1	spot size changed to 85 microns for all following NIST 610 analyses
3477	NIST 610	2	
3478	NIST 610	3	
3479	NIST 610	4	
3480	BIR-1G	1	
3481	BIR-1G	2	
3482	BIR-1G	3	
3483	BIR-1G	4	
3484	BIR-1G	5	
3485	BIR-1G	6	
3486	BIR-1G	7	
3487	BIR-1G	8	
3488	BIR-1G	9	
3489	NIST 610	1	

3490	NIST 610	2	
3491	NIST 610	3	
3492	NIST 610	4	
3493	BCR-2G	1	
3494	BCR-2G	2	
3495	BCR-2G	3	
3496	BCR-2G	4	
3497	BCR-2G	5	
3498	BCR-2G	6	
3499	BCR-2G	7	
3500	BCR-2G	8	
3501	BCR-2G	9	
3502	NIST 610	1	
3503	NIST 610	2	
3504	NIST 610	3	
3505	NIST 610	4	
3506	NIST 612	1	
3507	NIST 612	2	
3508	NIST 612	3	
3509	NIST 612	4	
3510	NIST 612	5	
3511	NIST 612	6	
3512	NIST 612	7	
3513	NIST 612	8	
3514	NIST 612	9	
3515	NIST 610	1	
3516	NIST 610	2	
3517	NIST 610	3	
3518	NIST 610	4	
3520	NIST 614	1	
3521	NIST 614	2	
3522	NIST 614	3	
3523	NIST 614	4	
3524	NIST 614	5	
3525	NIST 614	6	
3526	NIST 614	7	
3527	NIST 614	8	
3528	NIST 614	9	
3529	NIST 610	1	
3530	NIST 610	2	
3531	NIST 610	3	
3532	NIST 610	4	
3534	T1-G	1	85 micron spot size for this sample
3535	T1-G	2	

3536	T1-G	3
3537	T1-G	4
3538	T1-G	5
3539	T1-G	6
3540	T1-G	7
3541	T1-G	8
3542	T1-G	9
<hr/>		
3543	NIST 610	1
3544	NIST 610	2
3545	NIST 610	3
3546	NIST 610	4

Table A 1: Table with analysis numbers, sample name, and information on spot size to accompany the information shared in this thesis.

Appendix B

A Matlab script for the Monte Carlo simulation used to create data points for synthetic isochrons and calculate inferred ages is attached as `Almas_isochron.m`.

A Matlab script for calculating the slope, y-intercept, and uncertainties of these parameters was kindly shared by Madeline Raith and is attached as `f_Raith_York.m`.

Bibliography

- Albarède, F., Telouk, P., Blichert-Toft, J., Boyet, M., Agranier, A., & Nelson, B. (2004). Precise and accurate isotopic measurements using multiple-collector ICPMS. *Geochimica et Cosmochimica Acta*, 68(12), 2725–2744. <https://doi.org/10.1016/j.gca.2003.11.024>
- Anderson, F. S., Levine, J., & Whitaker, T. (2020). Dating a Martian meteorite with 20 Myr precision using a prototype *in-situ* dating instrument. *Planetary and Space Science*, 191. <https://doi.org/10.1016/j.pss.2020.105007>
- Arevalo, R., McDonough, W. F., & Piccoli, P. M. (2011). *In Situ* Determination of First-Row Transition Metal, Ga and Ge Abundances in Geological Materials via Medium-Resolution LA-ICP-MS. *Geostandards and Geoanalytical Research*, 35(2), 253–273. <https://doi.org/10.1111/j.1751-908X.2010.00099.x>
- Arevalo, R., Ni, Z., & Danell, R. M. (2020). Mass spectrometry and planetary exploration: A brief review and future projection. *Journal of Mass Spectrometry*, 55(1), e4454. <https://doi.org/10.1002/jms.4454>
- Benedix, G. K., Lagain, A., Chai, K., Meka, S., Anderson, S., Norman, C., Bland, P. A., Paxman, J., Towner, M. C., & Tan, T. (2020). Deriving Surface Ages on Mars Using Automated Crater Counting. *Earth and Space Science*, 7(3), e2019EA001005. <https://doi.org/10.1029/2019EA001005>
- Bibring, J.-P., Langevin, Y., Mustard, J. F., Poulet, F., Arvidson, R., Gendrin, A., Gondet, B., Mangold, N., Pinet, P., Forget, F., the OMEGA team, Berthe, M., Bibring, J.-P., Gendrin, A., Gomez, C., Gondet, B., Jouglet, D., Poulet, F., Soufflot, A., ... Neukum, G. (2006). Global Mineralogical and Aqueous Mars

History Derived from OMEGA/Mars Express Data. *Science*, 312(5772), 400–404. <https://doi.org/10.1126/science.1122659>

Cacopardo, A. (2020). A statistical analysis of the capabilities of LA-ICPMS as a prospective geochronology instrument for Rb-Sr dating. *UMD Geology Senior Thesis Archive*. 1-22.

Christensen, P. R., McSween, H. Y., Bandfield, J. L., Ruff, S. W., Rogers, A. D., Hamilton, V. E., Gorelick, N., Wyatt, M. B., Jakosky, B. M., Kieffer, H. H., Malin, M. C., & Moersch, J. E. (2005). Evidence for magmatic evolution and diversity on Mars from infrared observations. *Nature*, 436(7050), 504–509. <https://doi.org/10.1038/nature03639>

Cohen, B. A., Miller, J. S., Li, Z.-H., Swindle, T. D., & French, R. A. (2014). The Potassium-Argon Laser Experiment (KArLE): *In Situ* Geochronology for Planetary Robotic Missions. *Geostandards and Geoanalytical Research*, 38(4), 421–439. <https://doi.org/10.1111/j.1751-908X.2014.00319.x>

Cohen, B. (2020). Geochronology for the Next Decade. Presented at the meeting of the Mars Exploration Program Analysis Group, 04/16/2020.

Devismes, D., Gillot, P.-Y., Lefèvre, J.-C., Boukari, C., Rocard, F., & Chiavassa, F. (2016). KArMars: A Breadboard Model for *In Situ* Absolute Geochronology Based on the K–Ar Method Using UV-Laser-Induced Breakdown Spectroscopy and Quadrupole Mass Spectrometry. *Geostandards and Geoanalytical Research*, 40(4), 517–532. <https://doi.org/10.1111/ggr.12118>

Fahey, M., Yu, A., Grubisic, A., Getty, S., Arevalo, R., Li, X., Liu, R., & Mamakos, W. (2020). Ultraviolet Laser Development for Planetary Lander Missions.

2020 IEEE Aerospace Conference, 1–11.

<https://doi.org/10.1109/AERO47225.2020.9172711>

Farcy, B. J., Arevalo Jr., R. D., Taghioskoui, M., McDonough, W. F., Benna, M., & Brinckerhoff, W. B. (2020). A prospective microwave plasma source for *in situ* spaceflight applications. *Journal of Analytical Atomic Spectroscopy*, 35, 2740-2747. [https://doi-org.proxy-](https://doi-org.proxy-um.researchport.umd.edu/10.1039/DOJA00198H)

[um.researchport.umd.edu/10.1039/DOJA00198H](https://doi-org.proxy-um.researchport.umd.edu/10.1039/DOJA00198H)

Farley, K. A., Hurowitz, J. A., Asimow, P. D., Jacobson, N. S., & Cartwright, J. A. (2013). A double-spike method for K–Ar measurement: A technique for high precision *in situ* dating on Mars and other planetary surfaces. *Geochimica et Cosmochimica Acta*, 110, 1–12. <https://doi.org/10.1016/j.gca.2013.02.010>

Farley, K. A., Malespin, C., Mahaffy, P., Grotzinger, J. P., Vasconcelos, P. M., Milliken, R. E., Malin, M., Edgett, K. S., Pavlov, A. A., Hurowitz, J. A., Grant, J. A., Miller, H. B., Arvidson, R., Beegle, L., Calef, F., Conrad, P. G., Dietrich, W. E., Eigenbrode, J., Gellert, R., ... Team, the M. S. (2014). *In Situ* Radiometric and Exposure Age Dating of the Martian Surface. *Science*, 343(6169). <https://doi.org/10.1126/science.1247166>

Fialho, L. L., Pereira, C. D., & Nóbrega, J. A. (2011). Combination of cool plasma and collision-reaction interface for correction of polyatomic interferences on copper signals in inductively coupled plasma quadrupole mass spectrometry. *Spectrochimica Acta Part B: Atomic Spectroscopy*, 66(5), 389–393.

<https://doi.org/10.1016/j.sab.2011.04.001>

- Fietzke, J., Eisenhauer, A., Gussone, N., Bock, B., Liebetrau, V., Nögler, Th. F., Spero, H. J., Bijma, J., & Dullo, C. (2004). Direct measurement of $^{44}\text{Ca}/^{40}\text{Ca}$ ratios by MC–ICP–MS using the cool plasma technique. *Chemical Geology*, 206(1–2), 11–20. <https://doi.org/10.1016/j.chemgeo.2004.01.014>
- GeoReM: A New Geochemical Database for Reference Materials and Isotopic Standards. *Geostandards and Geoanalytical Research* 29 (3) [2005] 333-338.
- GEOROC (2021) Electronic database, Max Planck Institut für Chemie, Mainz, Germany. [Downloaded 25 June 2021.] Available from URL: <http://georoc.mpch-mainz.gwdg.de/georoc/Entry.html>
- Greeley, R., Kuzmin, R. O., & Haberle, R. M. (2001). Aeolian Processes and Their Effects on Understanding the Chronology of Mars. In R. Kallenbach, J. Geiss, & W. K. Hartmann (Eds.), *Chronology and Evolution of Mars* (Vol. 12, pp. 393–404). Springer Netherlands. https://doi.org/10.1007/978-94-017-1035-0_14
- Hartmann, W. K., & Neukum, G. (2001). Cratering Chronology and the Evolution of Mars. In R. Kallenbach, J. Geiss, & W. K. Hartmann (Eds.), *Chronology and Evolution of Mars* (Vol. 12, pp. 165–194). Springer Netherlands. https://doi.org/10.1007/978-94-017-1035-0_6
- Jenner, F. E., & O'Neill, H. S. C. (2012). Major and trace analysis of basaltic glasses by laser-ablation ICP-MS. *Geochemistry, Geophysics, Geosystems*, 13(3). <https://doi.org/10.1029/2011GC003890>
- Kelley, S. (2002). K-Ar and Ar-Ar Dating. *Reviews in Mineralogy and Geochemistry*, 47(1), 785–818. <https://doi.org/10.2138/rmg.2002.47.17>

- Maréchal, C. N., Télouk, P., & Albarède, F. (1999). Precise analysis of copper and zinc isotopic compositions by plasma-source mass spectrometry. *Chemical Geology*, 156(1–4), 251–273. [https://doi.org/10.1016/S0009-2541\(98\)00191-0](https://doi.org/10.1016/S0009-2541(98)00191-0)
- Martin, P. E., Farley, K. A., Baker, M. B., Malespin, C. A., Schwenzer, S. P., Cohen, B. A., Mahaffy, P. R., McAdam, A. C., Ming, D. W., Vasconcelos, P. M., & Navarro-González, R. (2017). A Two-Step K-Ar Experiment on Mars: Dating the Diagenetic Formation of Jarosite from Amazonian Groundwaters. *Journal of Geophysical Research: Planets*, 122(12), 2803–2818. <https://doi.org/10.1002/2017JE005445>
- McSween, H. Y., Grove, T. L., Lentz, R. C. F., Dann, J. C., Holzheid, A. H., Riciputi, L. R., & Ryan, J. G. (2001). Geochemical evidence for magmatic water within Mars from pyroxenes in the Shergotty meteorite. *Nature*, 409(6819), 487–490. <https://doi.org/10.1038/35054011>
- McSween, H. Y. & McLennan, S. M. (2014). 2.10. Mars. *Treatise on Geochemistry*. 10.1016/B978-0-08-095975-7.00125-X.
- Mustard, J. F., Poulet, F., Gendrin, A., Bibring, J.-P., Langevin, Y., Gondet, B., Mangold, N., Bellucci, G., & Altieri, F. (2005). Olivine and Pyroxene Diversity in the Crust of Mars. *Science*, 307(5715), 1594–1597. <https://doi.org/10.1126/science.1109098>
- National Aeronautics and Space Administration (2015). NASA Technology Roadmaps, TA8: Science Instruments, Observatories, and Sensor Systems. https://www.nasa.gov/sites/default/files/atoms/files/2015_nasa_technology_roadmaps_ta_8_science_instruments_final.pdf

- National Research Council (NRC) of the National Academies (2011). Vision and Voyages for Planetary Science in the Decade 2013-2022. *The National Academies Press*.
- Neukum, G., Ivanov, B., & Hartmann, W. K. (2001). Cratering Records in the Inner Solar System in Relation to the Lunar Reference System. *Space Science Reviews* 96, 86. <https://doi.org/10.1023/A:1011989004263>
- Neukum, G., & Horn, P. (1976). Effects of lava flows on lunar crater populations. *The Moon*, 15(3-4), 205-222. <https://doi.org/10.1007/BF00562238>
- Olesik, J. W. (2014). Inductively coupled plasma mass spectrometry. *Practical Spectroscopy Series*, 23, 67-158.
- Platz, T., Michael, G., Tanaka, K. L., Skinner, J. A., & Fortezzo, C. M. (2013). Crater-based dating of geological units on Mars: Methods and application for the new global geological map. *Icarus*, 225(1), 806-827. <https://doi.org/10.1016/j.icarus.2013.04.021>
- Poulet, F., Mangold, N., Platevoet, B., Bardintzeff, J.-M., Sautter, V., Mustard, J. F., Bibring, J.-P., Pinet, P., Langevin, Y., Gondet, B., & Aléon-Toppani, A. (2009). Quantitative compositional analysis of martian mafic regions using the MEx/OMEGA reflectance data. *Icarus*, 201(1), 84-101. <https://doi.org/10.1016/j.icarus.2008.12.042>
- (Raith, M., pers. comm. June 4, 2021)
- Rosman, K. J. R. & Taylor, P. D. P. (1999) IUPAC subcommittee for isotopic abundance measurements. *Pure Applied Chemistry*, 71, 1593-1607.

- Russell, W. A., Papanastassiou, D. A., & Tombrello, T. A. (1978). Ca isotope fractionation on the Earth and other solar system materials. *Geochimica et Cosmochimica Acta*, 42(8), 1075–1090. [https://doi.org/10.1016/0016-7037\(78\)90105-9](https://doi.org/10.1016/0016-7037(78)90105-9)
- Villa, I. M., De Bièvre, P., Holden, N. E., & Renne, P. R. (2015). IUPAC-IUGS recommendation on the half life of ^{87}Rb . *Geochimica et Cosmochimica Acta*, 164, 382–385. <https://doi.org/10.1016/j.gca.2015.05.025>
- Walker, R. J., Shirey, S. B., Hanson, G. N., Rajamani, V., & Horan, M. F. (1989). Re-Os, Rb-Sr, and O isotopic systematics of the Archean Kolar schist belt, Karnataka, India. *Geochimica et Cosmochimica Acta*, 53, 3005-3013.
- Werner, S. C., & Tanaka, K. L. (2011). Redefinition of the crater-density and absolute-age boundaries for the chronostratigraphic system of Mars. *Icarus*, 215(2), 603–607. <https://doi.org/10.1016/j.icarus.2011.07.024>
- Wordsworth, R. D. (2016). The Climate of Early Mars. *Annual Review of Earth and Planetary Sciences* 44:1, 381-408
- Patterson, K. Y., Veillon, C., David Hill, A., B. Moser-Veillon, P., & C. O'Haver, T. (1999). Measurement of calcium stable isotope tracers using cool plasma ICP-MS. *Journal of Analytical Atomic Spectrometry*, 14(11), 1673–1677. <https://doi.org/10.1039/A900677J>